Title

Soft Wearable Sensors for Continuous Cardiovascular Diseases Monitoring

Author

Qian, Chengyang

Publication Date

2024

UNIVERSITY OF CALIFORNIA,
IRVINE

Soft Wearable Sensors for Continuous Cardiovascular Diseases Monitoring

DISSERTATION
submitted in partial satisfaction of the requirements
for the degree of
DOCTOR OF PHILOSOPHY
in Biomedical Engineering
by
Chengyang Qian

Dissertation Committee:
Professor Michelle Khine, Chair
Professor Bernard Choi
Associate Professor Hung Cao

2024

DEDICATION

To:

My families, friends, and colleagues for their support and understanding.

TABLE OF CONTENTS

LIST OF FIGURES

ACKNOWLEDGEMENTS

I want to express my strongest and sincerest gratitude to my parents for giving birth to me, nurturing me, and supporting me. Without them, I would not be able to do meaningful things in my life, meet important people, write this thesis, and finish my Ph.D. journey. I also want to show my most grateful appreciation to Professor Michelle Khine for her understanding, support, and mentorship through this journey.

I am thankful to my classmates and colleagues, both from UCI and all the previous institutes that I attended. My classmates gave me opportunities to nourish and learn from each other in many aspects. My colleagues offered me unconditional help and guidance that supervisors cannot usually give. In retrospect, I will not be as experienced and knowledgeable without them.

I am also in debt to all my friends who put up with my complaints and negative emotions. Special thanks to Echo and Christopher since they saved me many times when my mind was about to collapse.

Lastly, I want to thank all the publishing groups for their permission to include many copyrighted figures and pictures in my thesis. For those people that I forgot to include in this acknowledgment, I still want to thank you all for helping me along the way.

VITA

Chengyang Qian

EDUCATION

2018	B.S. in Chemistry, Emory University, Atlanta, GA
2018	B.A. in Japanese, Emory University, Atlanta, GA
2020	M.S. in Materials Science and Engineering, University of Pennsylvania, PA
2024	Ph.D. in Biomedical Engineering, University of California, Irvine, CA

FIELD OF STUDY

Soft Wearable Sensors for Continuous Cardiovascular Diseases Monitoring

PUBLICATIONS

Qian, C., Rwei, P., Abiri, A., Zhou, Y., Chou, E., Tang, W. C., & Khine, M. (2022). Soft Iontronic Capacitive Sensor for Beat-to-Beat Blood Pressure Measurements. *Advanced Materials Interfaces*, *9*(18). https://doi.org/10.1002/admi.202200294. (**First Co-Author**)

Qian, C., Ye, F., Li, J., Tseng, P., & Khine, M. (2024). Wireless and Battery-Free Sensor for Interstitial Fluid Pressure Monitoring. *Sensors*, *24*(14), 4429.https://doi.org/10.3390/s24144429. (**First Author**)

Abiri, A., Chou, E. F., **Qian, C**., Rinehart, J., & Khine, M. (2022b). Intra-beat biomarker for accurate continuous non-invasive blood pressure monitoring. *Scientific Reports*, *12*(1). https://doi.org/10.1038/s41598-022-19096-6

Ye, F., Hajiaghajani, A., Zargari, A., Escobar, A., Qin, H., Li, L., **Qian, C**., Dia, K. K. H., Hasan, M. A., Dautta, M., Kurdahi, F., Khine, M., & Tseng, P. (2024). Passive Wireless Body Joint-Monitoring Networks with Textile-Integrated, Strongly Coupled Magnetic Resonators. *Advanced Electronic Materials*. https://doi.org/10.1002/aelm.202400450

Zhao, Q., Gouget, G., Guo, J., Yang, S., Zhao, T., Straus, D., **Qian, C**., Oh, N., Wang, H., Murray, C., & Kagan, C. (2021). Enhanced Carrier Transport in Strongly Coupled, Epitaxially Fused CdSe Nanocrystal Solids. *Nano Letters*, *21*(7), 3318–3324. https://doi.org/10.1021/acs.nanolett.1c00860

Qian, C., Li, J., Michelle Khine. Noninvasive Vital Signs Monitoring in the Neonatal Intensive Care Unit. *Sensors*. In preparation.

ABSTRACT OF THE DISSERTATION

Soft Wearable Sensors for Continuous Cardiovascular Diseases Monitoring
By
Chengyang Qian
Doctor of Philosophy in Biomedical Engineering
University of California, Irvine, 2024
Professor Michelle Khine, Chair

Wearable devices have the potential to revolutionize the healthcare industry. Due to their stretchability and/or flexibility, these devices can reach conformal contact with body parts that they are interfacing with. This property grants wearable devices more comfortable wearability and allows them to obtain high-quality signals, effectively enabling long-term wear and continuous monitoring of important information that is relevant to patients' health. This continuous information could be used for tracking, predicting, and preventing acute decompensation that typically requires timely treatment. The work presented here demonstrates a few wearable sensors that specifically focus on continuously monitoring vital signs useful for monitoring cardiovascular diseases, including rehabilitation. Specifically, a soft, capacitive sensor used for monitoring blood pressure, an LC-based sensor design used for tracking interstitial fluid pressure, and a wireless magnetic resonator-based network used for joint monitoring are presented in this dissertation.

CHAPTER 1: Introduction

1.1: Background on Wearable Sensors

The recent progress in the miniaturization of sensors has led to the ubiquity of the Internet of Things (IoTs), giving people vast amounts of data on many things of interest[1]. When these data are combined with all the machine learning algorithms, people can uncover many hidden insights that are otherwise not easily observable [2]. The same idea can also be implemented in the healthcare industry. In the context of the healthcare industry, different sensors can be placed on the body to acquire important and continuous physiological signals. Combined with machine learning algorithms, these continuous signals could be processed and used to uncover many hidden facts about people's health, effectively enabling the prediction, diagnosis, and monitoring of many chronic or acute diseases[3].

Traditional medical sensors are typically rigid and bulky, making them uncomfortable to wear for long periods and inconvenient for daily data collection. However, these obstacles can be bypassed via unconventional fabrication techniques, where the miniaturized sensors are made on flexible and/or stretchable substrates[4]. These resulting sensors can form conformal contact with the body parts they are interfacing with due to the flexible and/or stretchable substrates used. Due to the conformal contact, these wearable sensors are comfortable to wear for the long term and capable of streaming continuous data with high fidelity. To gather vital signs or biomarkers of interest, many wearable/ stretchable sensors were designed, as shown in **Figure** 1 [5]. In this dissertation, a few wearable sensor designs are proposed to specifically address the monitoring of cardiovascular diseases and subsequent rehabilitations.

Figure 1. Various wearable/ stretchable sensor designs used for collecting various vital signs and biomarker signals [5].

1.2: Background on Cardiovascular Diseases (CVD)

In this dissertation, the wearable sensors developed are intended to address cardiovascular diseases. Currently, cardiovascular diseases have become the number one cause of death worldwide, contributing 18.6 million deaths annually or one third of global deaths [6,7]. Despite its broad impact and lethality, most people are unaware of their cardiovascular conditions and hence, don't pay attention until a heart attack or stroke occurs, two sudden symptoms that are highly lethal and contribute to 85% of cardiovascular disease deaths [7–9]. These diseases in general are 'silent', relatively symptomless until an acute, often fatal, event. Broadly speaking, there are two types of cardiovascular diseases: vascular diseases and heart diseases (**Figure** 2)[10]. They have different causes and symptoms, implying different sensors should be developed for their respective monitoring.

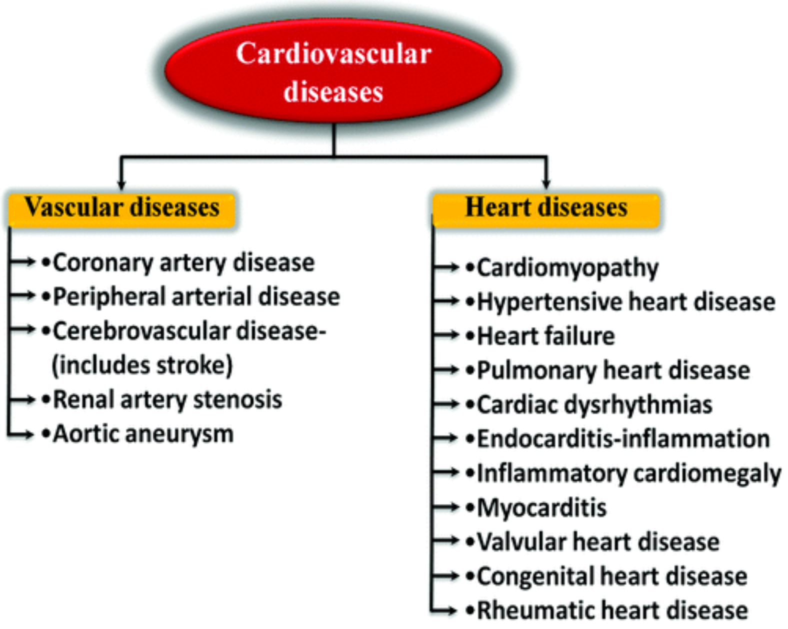

Figure 2. Two general types of cardiovascular diseases[10].

1.2.1: Vascular Diseases

Vascular diseases are a group of medical conditions that are related to the blood vessels and those blood vessels includes arteries, veins and capillaries. The presence of these diseases can disrupt or affect blood flow, which is responsible for delivering oxygen and nutrient to tissues and organs throughout the body. Metabolic wastes are also removed and carried away by the circulation of the blood. One of the common vascular diseases is atherosclerosis, a symptom of plaque buildup in arteries that lead to blood flow blockage and subsequent oxygen and nutrient deprivation in body tissues. Atherosclerosis can cause heart attack in the heart and lead to stroke in in the brain. Heart attack and stroke are two of the most acute and lethal resulting conditions and they often lead to sudden deaths if not treated on time. Generally speaking, risk factors for vascular diseases include smoking, unhealthy diet, obesity and sedentary lifestyle.

Blood pressure is an important indicator for vascular diseases, and hence, its continuous monitoring can offer meaningful trends for the onset. Blood pressures are often thought of as two important values: systolic and diastolic blood pressure. Systolic blood pressures are the maximum blood pressures due to the contraction of the heart's left ventricles, indicating how hard the heart is working. Diastolic blood pressures are the blood pressures recorded before the next heart contraction, indicating the overall resistance of the vascular system [11]. The presence of typical vascular diseases or their onsets can usually lead to abnormal blood pressures [12,13]. If blood pressures can be monitored continuously, then the presence or onset of vascular diseases can be detected and hence, treated on time.

For vascular diseases, high blood pressure (BP) is either the cause or the symptoms of those diseases, and therefore, BP is an important indicator. However, current blood pressure measurement is based on an armcuff that only gives one systolic and one diastolic value; it does not account for transient physiology or natural daily fluctuation [14]. Continuous blood pressure measurement accommodates those changes due to its beat-to-beat nature, and it is even recommended for definitive diagnosis of high BP, according to the American Heart Association[15,16].

The arterial line (A-line) is currently the best method for continuous BP monitoring at the moment. In this method, a catheter is inserted into the artery. However, due to its invasiveness, A-line needs to be placed by experienced professionals. Because of its potential complications, it is not suitable for everyday continuous monitoring. Many other noninvasive techniques exist, but they have their drawbacks[17]. Tonometry requires constant holding and alignment. The finger cuff volume clamp is extremely uncomfortable due to vasocontraction. To resolve the above problem, a sensor that is noninvasive, comfortable to wear, easy to align, and capable of continuous BP monitoring is developed.

1.2.2: Heart Diseases:

Heart diseases refer to congenital or disease-induced conditions that can affect the structure and function of the heart. One of the common heart diseases is cardiomyopathy, a condition that enlarge or stiffen heart muscle(myocardium). Other major common heart diseases include arrhythmias or valvular heart disease. These abnormalities in the heart structure reduce the heart's pumping efficiency, and can lead to the initiation of compensation mechanism, making the heart work harder to maintain sufficient blood flow to the body. Ultimately, prolonged overworking of the heart can ultimately lead to heart failure, an irreversible condition that leads to gradual, but permeant decrease in myocardial function. In the US, 6.7 million adults have heart failure, and the number is anticipated to increase to 8.5 million in 2030[18]. Most of the heart failure patients are older than 65 and African Americans are 20 times more likely to developed heart failure before 50. Although many heart diseases are congenital, there are many acquired risk factors such as smoking, hypertension, diabetes, obesity etc. [19]. There is currently no cure for heart failure, and this disease progresses in severity over time (**Figure** 3)[20]. The onset of heart failure usually causes a permanent reduction in myocardial function, significantly affecting patients' quality of life even after treatment. Close clinical follow-up of the disease leads to on-time treatment, causing more myocardial function to be retained after treatment. More heart function is even retained if the heart failure can be monitored continuously. Hence, a continuous monitoring method is preferred and needs to be developed.

Heart diseases ultimately lead to congestive heart failure (CHF). CHF is a detrimental condition that progresses over time even after treatment and, as such, deserves continuous attention. Clinically, heart failure monitoring is based on blood tests, EKG, or other visualization techniques. However, they are not convenient for continuous monitoring [21–26]. CardioMEMS can perform continuous monitoring of CHF, but it is costly and hard to install[27,28]. An alternative and practical biomarker named Interstitial fluid pressure (IFP) can be used for monitoring the onset of CHF, but it is frequently ignored. As CHF progresses, a failing heart is unable to pump enough blood, causing veins to have excessive blood accumulation and, subsequently, leakage of fluid from the capillary to the interstitium. The fluid buildup in the interstitium is, therefore, manifested as an increase in IFP and observable edema in the lower body.

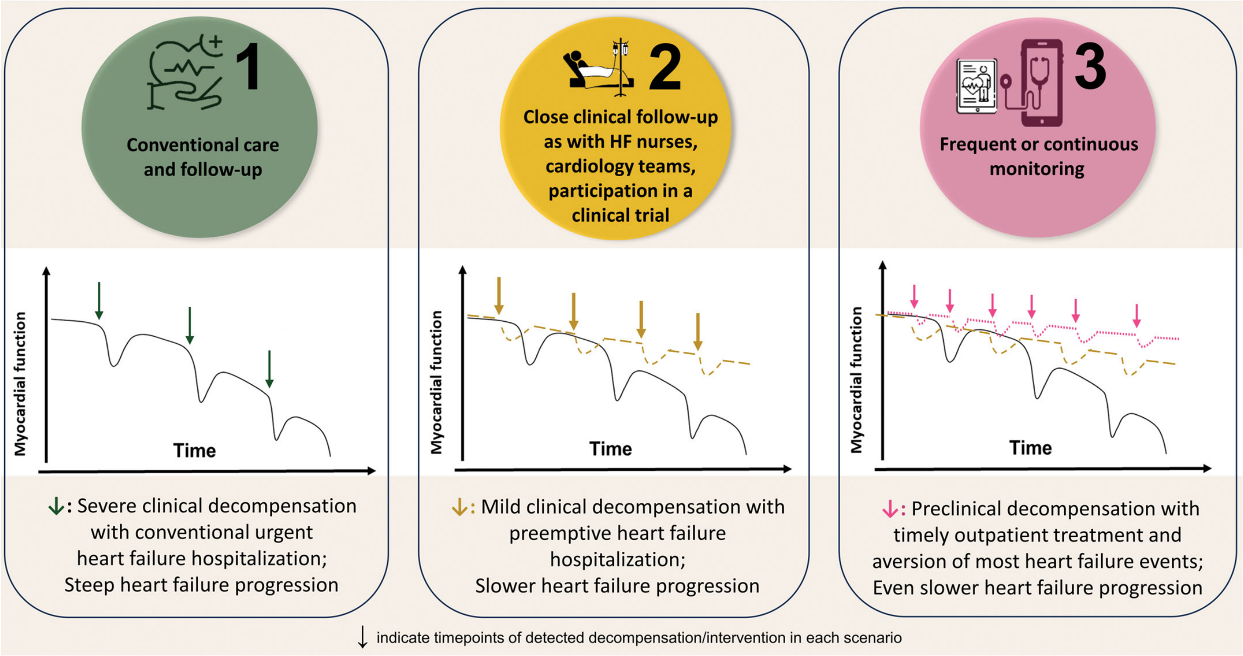

Figure 3. Different levels of myocardial function reduction using conventional, close follow-up, and continuous monitoring[20].

1.3: Dissertation Flow and Specific Sensor Designs

In **Chapter 2**, the materials and their processing are explained, and they are specifically used to make the wearable sensors explained in the subsequent chapters. A capacitive sensor that is noninvasive, comfortable to wear, easy to align, and capable of continuous BP monitoring is proposed and demonstrated in **Chapter 3**. The sensor possesses high sensitivity due to the wrinkled gold electrode, iontronic dielectric used, and the micro-ridge structure adopted. Using a bandpass filter and an initial BP measurement, the sensor's capacitance waveform can be converted to continuous BPs.

In **Chapter 4**, an inductor-capacitor sensor that can continuously monitor IFP is presented. The sensor can wirelessly transmit IFP information once implanted subcutaneously, and due to its inductive coupling sensing mechanism, the sensor can operate without any battery. Changes in IFP are quantified by the changes in resonance frequency of the implanted sensor.

A similar sensing mechanism shown in **Chapter 5** can also be implemented for sensing other types of information, with joint angle being one of them. Joint angle monitoring is important for gauging the biomechanical function and rehabilitation results for post-stroke patients. Post-stroke patients usually have paralyzed body parts, and one way to gauge their rehabilitation is through monitoring their joints' range of motion. The current methods for joint angle require demanding environmental light, clear line-of-sight, complicated equipment setup, and prior calibration[29]. In addition, some of them impede the motion of subjects and face the problem of mechanical failure due to repeated motion during measurement. In **Chapter 5**, a joint angle measurement mechanism that avoids the disadvantages of conventional methods is proposed. This mechanism utilizes strongly coupled magnetic resonators that are placed on two ends of a certain joint and quantifies joint angle changes based on the changes in system resonant frequency due to changes in coupling coefficient.

Finally, future prospects and directions in this field are discussed in **Chapter 6**.

CHAPTER 2: Material Selection and Fabrication for Wearable Sensors

Wearable electronics have attracted much interest in the field of healthcare[30–34]. Differing from traditional and rigid devices and sensors that impose stiffness mismatch with body surfaces, wearable sensors, and devices have flexibility and stretchability to form conformal contact with the body surface. Conformal contact provides better long-term wear comfort and higher signal quality. However, special materials and fabrication methods are needed to make those wearable devices.

2.1: Substrate Materials

Although there are many existing materials and structures for wearable sensors, most of them have a substrate layer and a conductive/functional layer on the substrate. [34–41] The Substrate layer is usually made of soft/flexible materials that ensure the final sensors will be wearable. The conductive/functional layer can accommodate strains from the substrate layer and still ensure the well-functioning of the sensor. The substrate materials and the conductive/functional materials used are explained in the following sections.

2.1.1: PDMS and Ecoflex

Polydimethylsiloxane (PDMS) is a promising substrate material for wearable sensors, and it is most widely used due to its soft mechanical properties and biocompatibility. PDMS has Young's modulus that ranges from 100 kPa to 3 MPa and can accommodate strain as big as 200%. These mechanical properties allow it to conform with the body and guarantee it is robust enough to tolerate many types of deformation. In addition, PDMS is chemically inert and biocompatible, making it safe for direct skin contact or implantation. Both its soft mechanical properties and chemical stability make PDMS an ideal substrate material for wearable sensors that are intended for continuous physiological monitoring. PDMS can also be prepared easily through the mixing of two types of monomers and used in soft lithography or replica molding. As such, microstructures can be created, and other functional elements can be incorporated. PDMS's surface can also be modified to improve adhesion, bonding, and integration of other sensing elements. All of the properties mentioned above make PDMS a versatile and indispensable substrate material for advancing wearable sensors.

Similar to PDMS, Ecoflex is another type of silicone material that is even softer. Ecoflex is softer than PDMS because of its lower crosslink density and the larger monomer side group. Lower crosslink density means less bond formation and larger monomer side groups mean loose packing of the polymer chains. Both ensure the material's softer mechanical properties.

2.1.2: Polyimide or Kapton

Polyimide or Kapton is another promising substrate material for wearable devices. Kapton is less stretchable and harder than elastomeric materials such as PDMS or Ecoflex, making it less ideal for sensors that demand high elasticity or significant deformation. Kapton does possess certain flexibility and biocompatibility; it is frequently used as a bonding material to mitigate the stiffness mismatch between two types of materials[42]. Some manufacturers even provide double-sided Kapton tapes, an even better option for bonding different materials.

2.2: Conductive/Functional Materials

Early wearable sensors adopt conductive metal with special surface geometries to account for strains, and serpentine is the most common one being adopted[34,36,37,39,43,44]. One of the structures, named Miuraori, is said to increase the substrate stretchability by 75% [40]. However, the fabrication of those structures and the material add extra complexity to the fabrication, use, functionality, and lifetime of the final product. Embedding conductive material in elastomers is an alternative approach to make conductive layers[45–47]. However, this type of conductive layer suffers a decrease in conductance when stretched and therefore, is mostly used for strain sensors. Liquid metal is an alternative material that can serve as a good conductive layer[36,38]. However, channels filled with liquid metal need extra precaution and handling during fabrication and can cause leakage due to mechanical failure.

2.2.1: Wrinkled Gold as Conductive/Functional Material

Over the years, conductive layers on stress-relief wrinkled structures have been shown to be capable of accommodating changes in strain when being stretched[30,34,48,49]. Methods have been introduced to produce gold wrinkle structure on PDMS/Ecoflex wearable substrate, demonstrating good stretchability and robustness as a type of conductive layer. The fabrication process starts with pre-stress polystyrene, a shape memory polymer that shrinks to 1/3 of its original size when heated to its glass transition temperature. If the metal film is deposited on the polymer and then heated, the thin metal film will buckle, and form wrinkled structures due to the stiffness mismatch between the polymer and the metal film. The wrinkled gold can be further transferred onto PDMS/Ecoflex silicone after surface treatment, and the resulting structure is proven to retain its high conductivity at 200% strain[50].

2.2.2: Copper Foil as Conductive/Functional Material

Thin film is usually more flexible than its bulk form and hence, more suitable to be used for wearable sensors. Copper is one of the most conductive metals, and its foil is widely available. Copper's high conductivity makes it highly desirable for the conductive path or wearable antenna. Both applications require low resistance. Although copper in foil form is not stretchable, it is flexible and, thus, can accommodate bending. Therefore, it is more suitable for sensors that are only bent but not stretched. The thin copper foil is also ideal for subtractive processes such as cutting using a craft cutter or a laser. The same process cannot be performed on thicker copper plates. Through proper encapsulation, copper can resist oxidation and is safe for direct body contact.

2.3: Fabrication Techniques

Some of the fabrication techniques used in the current semiconductor industry can be directly adopted for the fabrication of wearable sensors. Common techniques include sputtering for metal deposition and etching. Some of the uncommon techniques used in the dissertation include laser ablation and craft cutting.

2.3.1: Metal Sputtering

Metal deposition through the processing of sputtering is a physical vapor deposition process that involves bombarding atoms from a metal target and coating the metal on a substrate. In the process, the sputtering chamber is usually filled with Argon gas, and those Argon atoms become ionized due to the presence of an electric field[51]. The resulting ion will bombard the metal target, such as gold, and those metal atoms will be knocked down and land on the sample substrate. The sputtering process can be achieved at room temperature, which is ideal for pre-stressed polystyrene that can shrink at elevated temperatures. The deposited metal can also have desired patterns if a frisket film is used to selectively cover certain areas.

2.3.2: Metal Pattern Transfer

After the process of heat-induced shrinking of polystyrene, the wrinkled metal pattern needs to be transferred onto wearable substrates such as PDMS or Ecoflex. The substrate needs to be treated with a layer of molecular glue so that the metal layer can attach to PDMS and remain on PDMS after the removal of the polystyrene layer. The substrate is treated in ethanol that has 0.005 M of (3-mercaptopropyl) trimethoxysilane (MPTMS) for 2 hours.

PDMS is prepared by mixing the two types of monomers in a weight ratio of 1:1 and spin-coated onto the treated substrates before curing. The process of spin-coating can result in an evenly coated layer of liquid material, and the thickness depends on the speed of rotation. The resulting substrates are treated in a vacuum chamber so that liquid PDMS can fill the wrinkles and firmly bond with MPTMS. Finally, PDMS is cured at elevated temperatures.

The polystyrene needs to be removed so that only gold can remain on the PDMS. The process of polystyrene removal is done through the process of etching, a subtractive fabrication procedure. The polystyrene is removed through the process of wet etching. The substrate is immersed in an organic solution bath at an elevated temperature so that the polystyrene can be dissolved. Substrates are immersed in acetone at 75 Celsius for 20 minutes so that PDMS with gold can be peeled off. The PDMS is then immersed in toluene solution for 2 minutes and sonicated for further cleaning. The resulting substrate is dried at room temperature.

2.3.3: Oxygen Plasma Cleaning and Surface Activation

There is residue organic contamination on the surface of the electrode, and the contamination can be removed using oxygen plasma. It works by exposing the contamination to ionized oxygen gas with high-energy oxygen species, such as ions and radicals. These high-energy species can break the bonds in organic species and decompose them into smaller molecules that can detach from the surface more easily. In addition, these species can break bonds in PDMS or Ecoflex surfaces and create surface radicals that can bond with other radicals or molecules. These radicals can bond two pieces of substrates, providing an effective assembly method. Hence, oxygen plasma is an effective way for cleaning and surface bonding.

2.3.4: Laser Ablation

Laser ablation is a subtractive fabrication technique that has gained significant attention due to its precision and versatility. The technique uses a focused laser beam to raster a material surface to define a specific shape or cut a specific material into a defined shape. The laser's interaction with the surface depends on the laser's wavelength, speed, and power. Laser ablation is popular due to its high resolution and precise control of material removal, making it suitable for defining our sensor's electrode or conductive path shape.

2.3.4: Craft Cutting

Craft cutting is another subtractive process that involves the use of a blade to directly cut a certain material into the desired shape. The important parameters include the force, speed, and length of blade protrusion. A correct combination of speed, force, and blade protrusion ensures the blade only cuts the surface material but not the substrate material that is on the bottom. Craft cutter provides a subtractive fabrication method that is supplementary to laser ablation. Lasers with longer wavelengths are not suitable for cutting metal surfaces since the metal's smooth surface can reflect the laser light. Despite the craft cutter’s lower precision, it can provide a rapid alternative method for patterning the metal without worrying about light reflection.

CHAPTER 3: Ultra-Sensitive Capacitive Sensor for Continuous Blood Pressure Measurement

3.1: Background and Motivation

Vascular disease is one category of cardiovascular disease. Blood pressure (BP) is highly indicative of many potential or ongoing vascular diseases. Blood pressures are composed of two important values: systolic and diastolic blood pressure. Systolic blood pressures are the maximum blood pressures due to the contraction of the heart's left ventricles, indicating how hard the heart is working. Diastolic blood pressures are the blood pressures recorded before the next heart contraction, indicating the overall resistance of the vascular system [11]. The presence of typical vascular diseases or their onsets can usually lead to abnormal blood pressures [12,13]. However, BP values naturally oscillate, spanning from short-term beat-to-beat variability to long-term 24-hour circadian fluctuation, making it challenging to decouple many confounding factors and detect the actual abnormalities associated with vascular diseases. As such, an accurate diagnosis cannot be made. BP monitoring is usually obtained from an armcuff or sphygmomanometer, devices that can only provide single-value measurement and therefore, cannot discriminate momentary physiological state from chronic conditions. Ambulatory BP monitoring (ABPM) has received more and more attention over the past 20 years since it avoids the shortcomings of single-value measurement and can provide more insight into cardiovascular diseases as an independent risk factor[14]. To give an example, according to the American Heart Association, ABPM is recommended for the definitive diagnosis of high BP, and this process requires multiple blood pressure taken in 24 hours so that the individual's daily activities are taken into consideration. It has already been proven that ABPM provides a more holistic view of a patient's cardiovascular condition and is more accurate in hypertension detection compared to other clinical methods[15,16].

However, ABPM is still based on oscillometric methods that only provide averaged BP values over periods of 30 to 40 seconds and require subjects to stay still during measurement for optimal recording[52–54]. As such, it still does not capture BPs with the finest resolution. So far, the arterial line is the standard method for continuously monitoring beat-to-beat BPs. In this method, a catheter is inserted inside the artery, and the pressure sensor in the catheter is responsible for continuous pressure sensing in the artery. Nevertheless, arterial lines are usually used on high-risk patients in the intensive care unit since they are invasive, face complication risks, and require experienced personnel for installation.

Many noninvasive BP monitoring options exist, but they all have their respective drawback. The finger cuff method can be uncomfortable to wear and is easily affected by vasoconstriction in peripheral arteries[53–55]. Applanation tonometry must be positioned on top of the artery constantly during measurement and therefore, is not suited for continuous BP measurement[53,56].

To bypass the limitations of the methods mentioned above, a wearable and ultra-sensitive BP sensor needs to be developed. Many existing wearable sensors adopt a capacitive sensing scheme for its simple design and easy integration on common wearable substrates. This sensing scheme is also good at dynamic responses compared to other pressure sensing methods [57–75]. However, current capacitive sensors lack sensitivity, have slow response time, and are limited in both dynamic range and anti-noise capability. Despite the utilization of various microstructures to improve response time and sensitivity, the resulting sensors still only have high sensitivities over small pressure ranges[76–85].

In this chapter, an improved capacitive sensor with several innovations is demonstrated. In this new sensor, a conventional dielectric material is changed to an iontronic dielectric, and micro-ridge structures are added to the sensor's substrate through micromachining. The resulting sensor has ultra-sensitivity over a large dynamic range. The use of iontronic material encourages the formation of electrical double layers that increase the baseline capacitance so the effect of electromagnetic noise can be reduced. Daisy-chain-shaped electrodes are also designed so that the sensor forms multi-islands after assembly. This design not only enables easy alignment with the radial artery but also retains the sensor's good response time and high noise resistance. Finally, the sensor is demonstrated to be capable of performing continuous BP monitoring. Using a one-time BP measurement from an armcuff and a bandpass filter, the BP waveform obtained from the sensor can be converted to continuous BP values with high fidelity.

3.2: Sensor Overview and Fabrication

3.2.1: Overview

The pressure sensor is made of two pieces of polydimethylsiloxane (PDMS) that have daisy-chain-shaped electrodes with micro-wrinkles. PDMS is used as the substrate material because of its suitable mechanical property that allows the sensor to form conformal contact with the body and encourages wearability[86]. A layer of iontronic material exists between the electrodes and is used as the dielectric material. An Ecoflex layer is incorporated to facilitate the bonding of two PDMS substrates after being treated with oxygen plasma. The orthogonal orientation of two electrodes forms a multi-island design after assembly. The electrodes have gold wrinkles that have been demonstrated to maintain electrical conductivity under 200% strain[50,87]. As such, the wrinkled structure ensures the sensor is robust even when it is integrated into soft elastomeric PDMS. The detailed sensor layout is demonstrated in **Figure** 4.

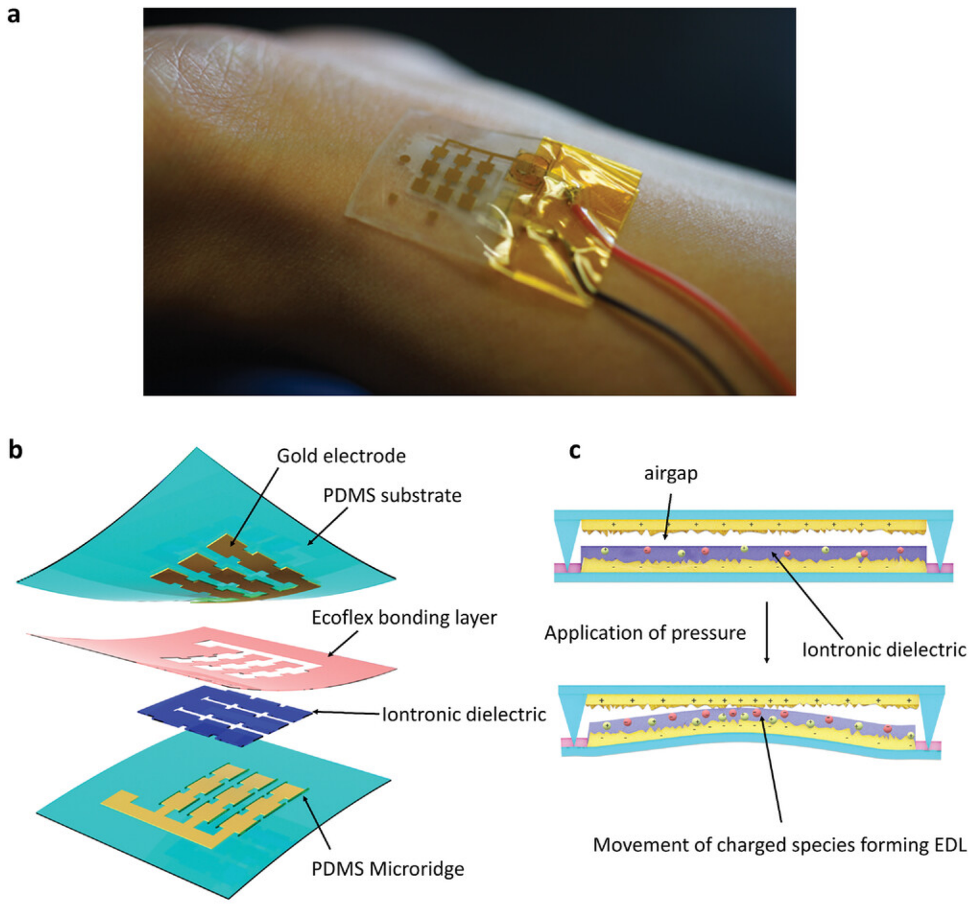

Figure 4. Capacitive sensor demonstration. (a) A picture of the sensor positioned on the radial artery. (b) A detailed sensor structure. (c) Electrical double layer formation within the iontronic material.

The iontronic material is chosen as dielectric material to boost the sensor's sensitivity. When electrodes are brought into contact, charged ions in the iontronic dielectric can migrate to their respective electrode and form an electrical double layer (EDL), a phenomenon that boosts both the baseline capacitance and the change in capacitance[88]. Micro-ridges exist on the two sides of each square pad, and they create an air gap between each square pad pair. Initially, the electrodes are not touching the iontronic dielectric, and hence, EDLs cannot form, and therefore, the baseline capacitance is low for the sensor. The following equation defines the sensitivity of a capacitive sensor:

$$S = \frac{\frac{\Delta C}{C_0}}{P} \tag{1}$$

where C_0 is the baseline capacitance, ΔC is the capacitance change due to pressure applanation, and P stands for the applied pressure. Due to the low baseline, the sensitivity is enhanced since every capacitance change will be more significant with respect to an already small baseline.

3.2.2: Sensor Fabrication

60 nm of gold was sputtered on a pre-stressed polystyrene (PS) polymer substrate. The substrate was placed in an oven at 140 $°C$ for 10 minutes so that the pre-stressed PS could shrink. The stiffer gold on the PS formed wrinkled gold microstructures due to shrinking and buckling with the PS substrate. The shrunk substrate was raster by a CO_2 laser to define the daisy-chain-shaped electrode (speed 84% and power 13%). On one of the shrunk PSs, microgrooves were defined at two edges of all the square electrode pads at 2.5% speed and 2% power. After the definition of microgrooves and electrodes, the substrates were treated with ethanol that contained 0.005 M of (3-mercaptopropyl) trimethoxysilane (MPTMS) for 2 hours. This ensured PDMS would bond onto the gold wrinkle at the subsequent electrode transferring steps. After the substrates were dried and rinsed, PDMS was spin-coated onto the substrates. The substrates with spin-coated PDMS were placed in a vacuum environment for 20 minutes at -96 kPa pressure so that PDMS could flow into the microstructure. Later, the substrates were left in an oven for 2 hours, and the temperature was set to 60 $°C$ so that PDMS could solidify. The substrates were treated with acetone for 20 minutes at 75 $°C$ so that PS polymer could be dissolved and PDMS could be peeled off with gold electrode being transferred onto PDMS. The PDMS was finally treated with toluene for 2 minutes with sonication so that the residual PS could be removed.

A frisket film pattern was defined by a laser cutter so that it could serve as a mask that selectively cover the electrode on the substrate that did not have any micro-ridges. Ecoflex 0030 was spin-coated on the PDMS to facilitate the bonding of two substrates. The frisket mask was removed before the curing of Ecoflex so that the electrode remained uncovered. As a result, electrodes could form direct contact with the iontronic dielectric. The remaining Ecoflex layer promoted the plasma bonding of PMDS substrates that were otherwise wrinkled and hard to bond. The iontronic dielectric was spin-coated on the flat substrate and cut into the shape of the electrode. In the end, substrates were placed orthogonal to each other and assembled together using oxygen plasma for 60 seconds at 200 mTorr. The sensor fabrication step is demonstrated in **Figure** 5.

The iontronic dielectric was made from 1-ethyl-3-ethyl-methylimidazolium bis(trifluoromethylsulfonyl) amide and poly (vinylidene fluoride-co-hexafluoropropylene) with a weight ratio of 1:1 for optimal performance. The ratio was demonstrated to offer the largest areal capacitance for input potential with various frequencies[89,90]. The mixture was heated in acetone at 75 $°C$ until everything was completely dissolved. Before being used, the mixture was cooled until reaching room temperature.

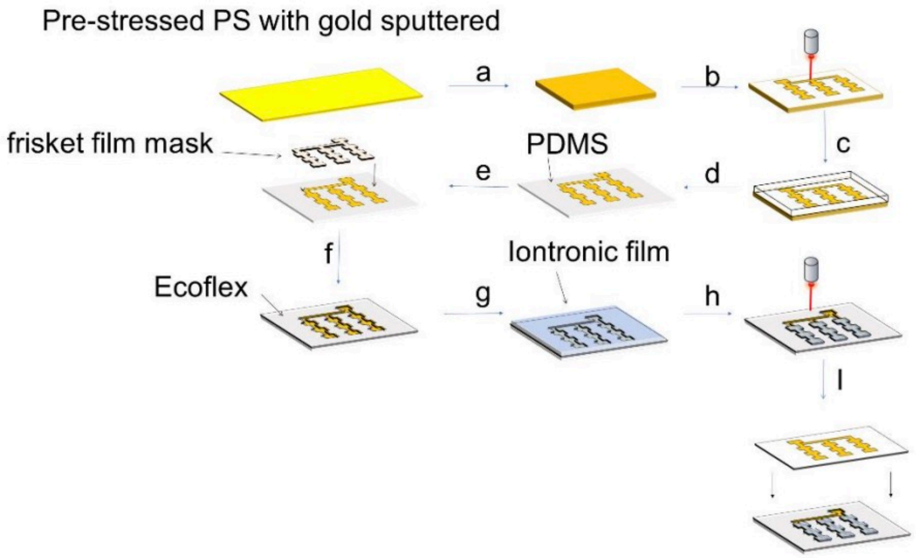

Figure 5. The process flow for soft iontronic capacitive sensor fabrication. (a) Shrinking of the PS substrate at 140 Celsius for 10 minutes. (b) The pattering of the electrode and microgrooves using a laser cutter. (c) MPTMS treatment, PDMS spin-coating, and vacuuming. (d) PS solvation for gold electrode pattern transferring. (e) Definition of frisket film mask for covering the electrode. (f) Spin-coating of Ecoflex and removal of the mask before Ecoflex curing. (g) Spin-coating of iontronic dielectric. (h) Iontronic dielectric laser patterning. (i) electrodes assembly after oxygen plasma treatment.

3.3: Sensor Characterization

3.3.1: Sensitivity

Normal force was applied through a piece of acrylic square using a force gauge that was connected to a test stand. The square acrylic probe was 8 mm in edge length so that its size was enough to overlap the sensor's sensing area. The pressure applied to the sensor was calculated using the force gauge reading and acrylic tip area. The change in capacitance due to applied normal forces was captured using an LCR meter, and the resulting sensitivity was calculated using Equation (1).

The resulting sensor was shown to have averaged sensitivities of 108.52 kPa^{-1} from 0 to 5 kPa and 14.95 kPa^{-1} from 5 to 25 kPa at 10 kHz input potential frequency (**Figure** 6a). Compared with other capacitive sensors, our sensor demonstrated higher and more linear sensitivity over a broader pressure range, making the sensor suitable to our purposes of ensuring the sensor can operate with high sensitivity despite the use of applanation pressure above the artery[30,77,85,89–100]. The sensor had different sensitivities at different input potential frequencies since AC potential cause the migration and oscillation of the charged ions in the iontronic material. At low frequencies, the charged ions had more time to move toward the corresponding electrode and therefore, form more complete EDLs compared to those that were driven at higher input frequencies. EDLs formed under low input frequency correspond to bigger capacitance change and therefore, higher sensitivities[101–103]. The sensor could be tuned to be used for other applications that have different requirements by simply changing the input frequencies. As shown in **Figure** 6a, the sensor sensitivity decreased to 4.68 and 1.13 kPa^{-1} at their respective pressure ranges at 300 kHz, respectively. Despite the lower sensitivity, 300 kHz was still selected for BP measurements since its optimal sampling rate led to waveforms with high resolution.

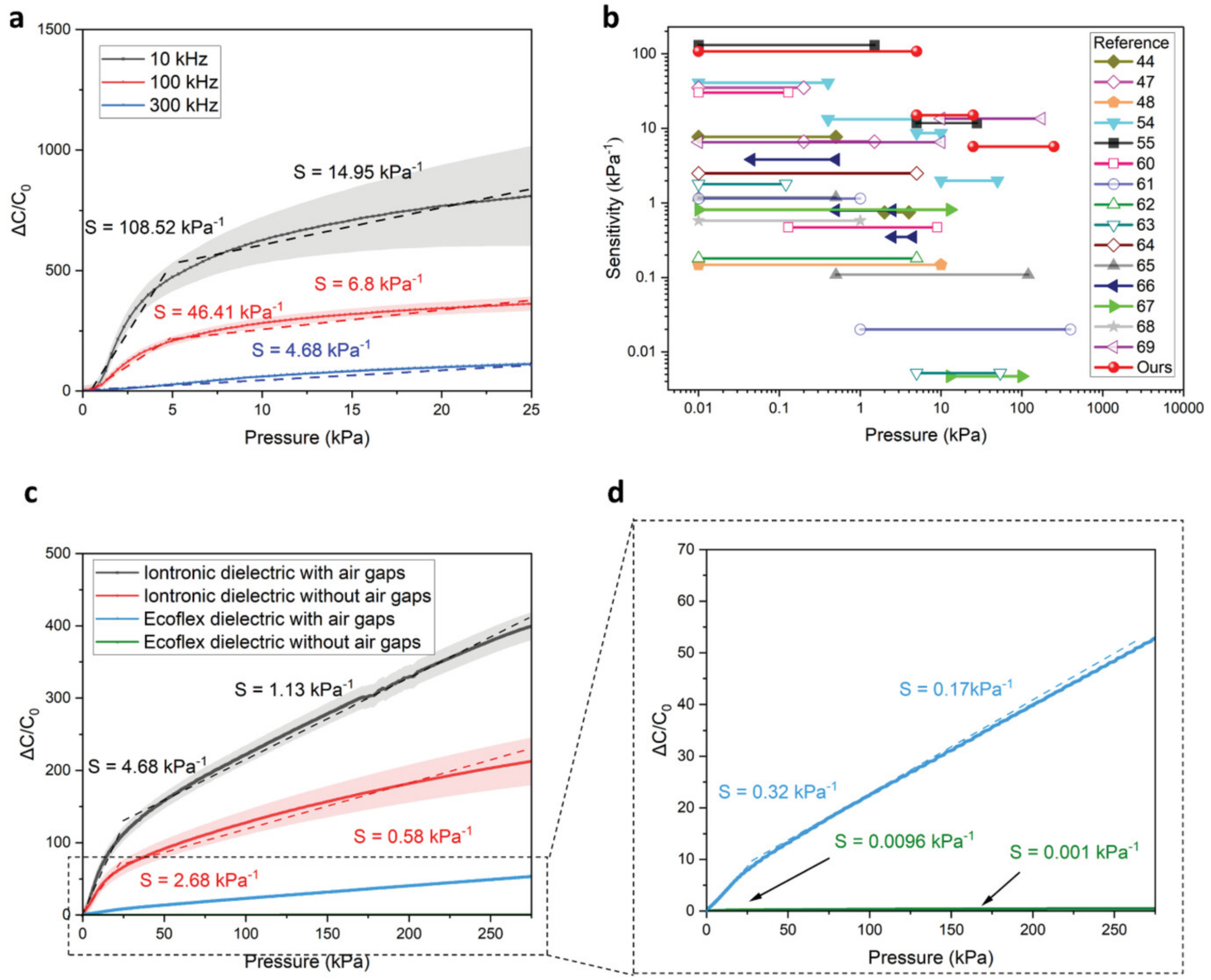

Figure 6. Averaged sensor sensitives at different conditions. (a) Sensitivities at different input potential frequencies (n=5). (b)Our sensor's sensitivities and different dynamic ranges compared with other published sensors. Refer to the publication for the number listed in the figure. (c) Different Sensors' sensitivities at different frequencies 300 kHz. (d)Zoomed-in sensitivities are shown on the right.

The role of iontronic dielectric and air gap in enhancing the sensitivity was also scrutinized. The presence of iontronic dielectric enhanced the change in capacitance due to the displacement of charged species forming EDLs when electrodes were brought close to each other [88]. According to **Figure** 6c, the sensor that used iontronic materials as dielectric showed enhanced sensitivity. The presence of air gaps further contributed to the sensitivity of the sensor due to its ability to lower the baseline capacitance, causing every change in capacitance to be more significant with respect to an already low baseline. Also shown in **Figure** 6c, the control groups that lack air gaps had lower sensitivity since the electrodes were already contacting iontronic dielectric, forming EDLs that increased the baseline capacitance at the sensor's resting state. Due to the use of iontronic dielectric material, incorporation of air gaps, and the use of wrinkled electrodes, our sensor demonstrated ultrahigh sensitivity compared with other published sensors (**Figure** 6b). In fact, the only sensor that had higher sensitivity than us used acid to provide charged ions in the dielectric material. Due to the possible corrosion acid can cause, it is less ideal than the ionic liquid material we used. In addition, our sensor had a higher dynamic range at its highest sensitivity due to the micro features added to our design. This indicated that our sensor is likely to operate with its highest sensitivity despite the use of applanation pressure.

3.3.2: Response Time and Fatigue Test

A square mechanical input was given using a motor so that the sensor's response time could be obtained. The sensor's capacitance change versus time responses were also obtained using an impedance analyzer that could capture 899 data points per second. The sensor was compressed by 0.3 mm, and the corresponding actuation time was captured as well. The response time was obtained by subtracting the actuation time from the sensor's reaction time to reach strain-induced maximum capacitance. Based on the results obtained from five square waves, an average response time of 55.8 ± 1.8 ms was determined (**Figure** 7 a and b). This averaged response time indicated that the sensor could record the BP waveform with sufficient resolution, given that a normal adult has a resting heart rate ranging from 60 to 90 beats per minute.

The sensor's durability was also verified via a fatigue test. The sensor was compressed by 50 kPa pressure for 5000 cycles. Consistent capacitance changes and stable capacitance baseline were observed during this test. This suggested that the sensor has sufficient robustness to provide reliable measurement for a long time.

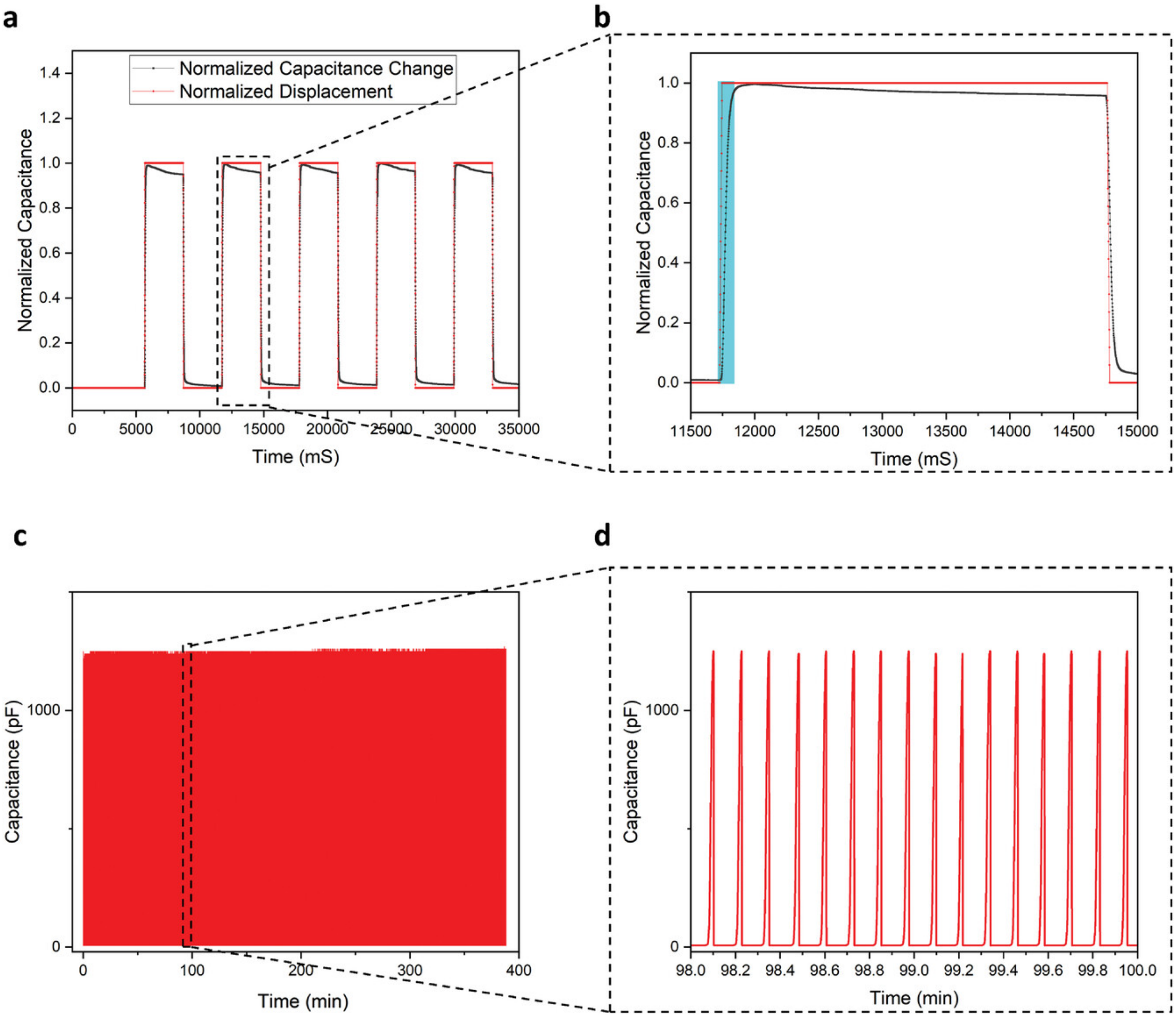

Figure 7. Response time and fatigue test of the sensor. (a) The five square waves are used for obtaining response time. (b) One of the zoomed-in square waves. (c) Fatigue test of the sensor over 5000 cycles of compressive pressure. (d) Zoomed-in fatigue test cycles.

3.4: In-Vivo Continuous Blood Pressure Measurement Results

3.4.1: Sensor Placement for blood pressure monitoring

To ensure ease of use, the sensor's electrode shape was specifically designed to be daisy-chain so that the assembled sensor could form multi-island geometry. It bypassed the shortcoming of typical tonometry, where the transducer has to be accurately aligned above the artery, and the misalignment can easily occur due to small movements. To verify the ease of use of this sensor design, a phantom BP generation device that was able to generate pseudo pulses was designed.

Pseudo pulses were generated by a pump that was connected to Arduino. On the phantom device, a grided line with intervals of 1 mm was drawn, and it was centered over the phantom's artery. Both the current and old sensors were positioned on the phantom and aligned with different grid lines using an applanator (**Figure** 8). The waveforms were recorded for both the current and old sensor design at each grided line, with the center of each sensor aligned on top of it. As shown in **Figure** 8 c, our current sensor was found capable of detecting pulsatile pressure despite its gradual misalignment from the "artery". In contrast, the previous design began to capture inverted waveforms due to misalignment. Additionally, the signal amplitude captured by the current sensor was a lot larger than that from the old design. As such, the electrode's daisy-chain shape and each island's high sensitivity ensure the capture of waveform despite its misalignment with the artery and therefore, contribute to the sensor's ease of use.

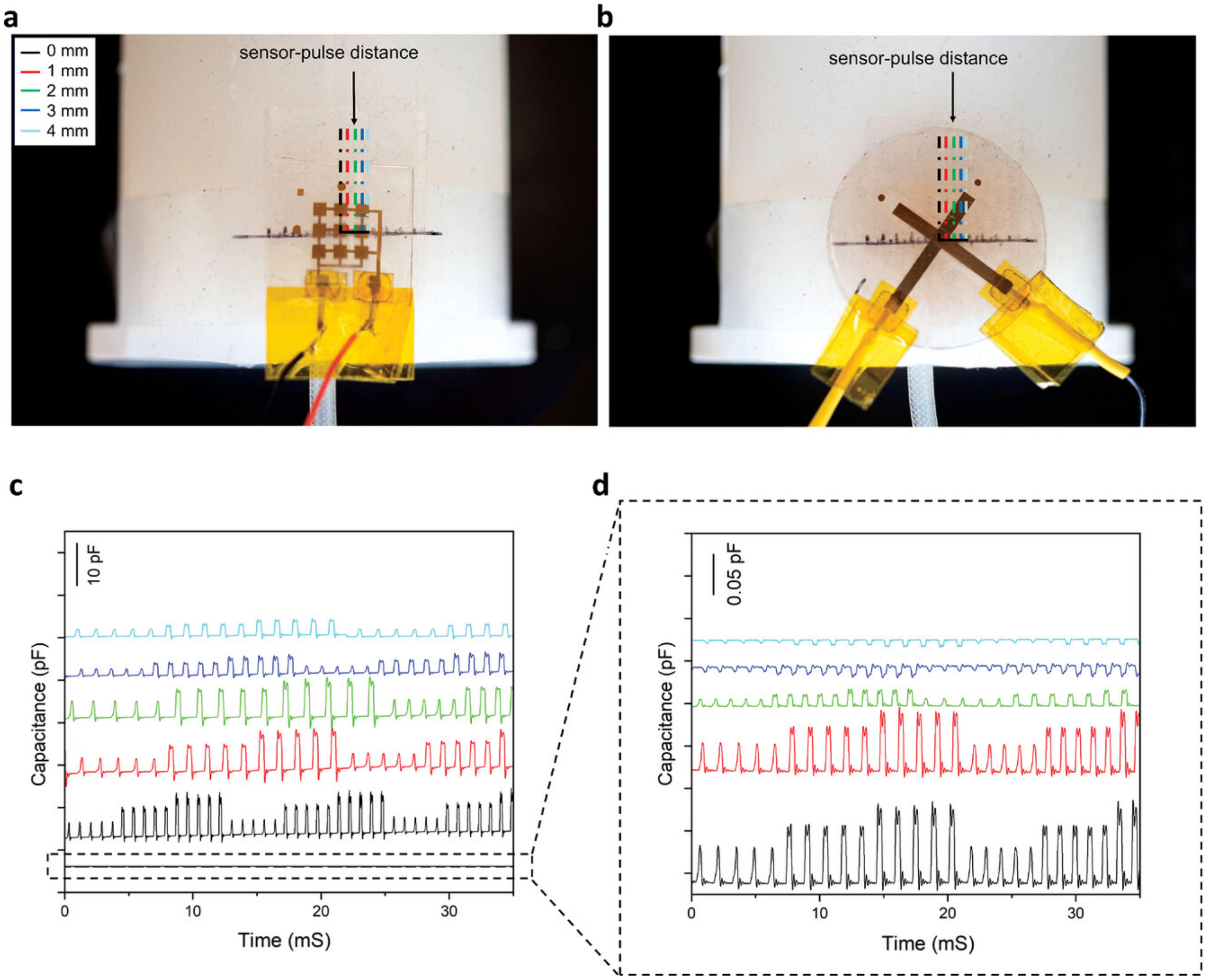

Figure 8. The alignment test on phantom using the current and old sensor design. (a) Alignment of the current sensor with the grided line (b) Alignment of the old sensor with the grided line. (c) Pseudo waveforms from the current sensor (scale bar = 10 pF). (d) Pseudo waveforms from the old sensor scale bar = 0.05 pF).

3.4.2: Continuous BP Monitoring

The sensor was connected to an LCR meter and positioned above the radial artery with an applanator so that continuous BP waveform could be captured. At the same time, a device named Caretaker was used to capture BP values, including both systolic and diastolic pressures. Both the sensor and the Caretaker were calibrated using an inflatable armcuff that provided one-time systolic and diastolic pressure. Waveforms were captured from six subjects on radial artery using the sensor, and the sensor was held still using an applanator. The experimental setup is shown in **Figure** 9a. Both devices started recording simultaneously, and the recording lasted for 10 minutes. During the process, all subjects were staying still and kept both devices at heart level. The waveforms from both devices were normalized and are shown in **Figure** 9b. The normalized waveform was filtered using a 4th-order Butterworth bandpass filter. Cutoff frequencies were set to 0.5 and 10 Hz since this frequency range removes baseline wandering and high-frequency noise.

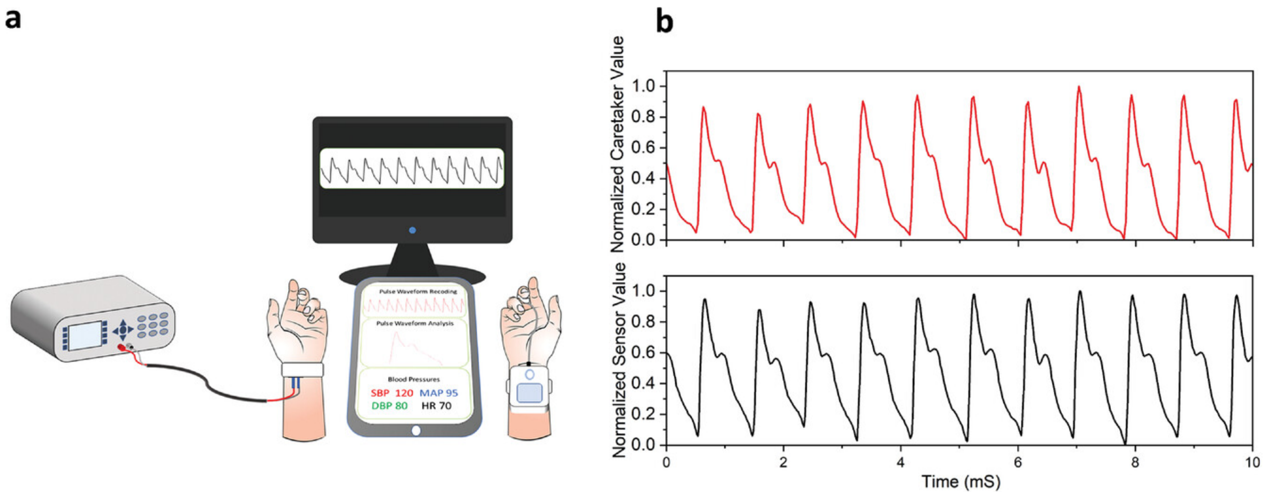

Figure 9. Experimental setup and the corresponding waveforms. (a) The sensor and the Caretaker setup for recording continuous blood pressure. (b) Waveforms captured by both devices.

A one-time BP was obtained from an armcuff, and a transformation factor was derived to convert capacitance waveforms to BP waveforms. Systolic BPs and diastolic BPs were the peaks and valleys of waveforms, and they were used to derive mean arterial pressure using the following equation:

$$MAP = \frac{1}{3}SBP + \frac{2}{3}DBP$$

For demonstration, systolic BPs, diastolic BPs, mean arterial pressures, and heart rates obtained from the sensor and those from the Caretaker were compared for one of the subjects (**Figure** 10 a and b). The sensor values were able to corroborate with the Caretaker values.

The waveforms from both devices also had high similarities. The waveforms from the sensor and the Caretaker were adjusted to the same sampling frequency, and then, the resulting waveforms were separated into individual pulses. Then, Pearson Correlation analysis was done on the individual pulse captured by both devices for one subject after normalization and alignment (**Figure** 10 c). The total Coefficient was divided by the total peak number, and the average coefficient was 0.964.

Bland-Altman analyses were performed on systolic, diastolic, and mean arterial pressures that were obtained from both devices for all the experimental subjects (**Figure** 10 d-f). The mean biases and standard deviations were 0.48±5.57, 1.43±3.66, and 1.59±2.96 mmHg for systolic, diastolic, and mean arterial pressure, respectively. The results met the standard of the Association for the Advancement of Medical Instrumentation, where the mean bias should be less than 5 mmHg, and the standard deviation should be less than 8 mmHg [52,104]. In summary, the sensor could perform continuous BP measurements with high accuracy. Compared to those methods that require two devices (pulse arrival time and pulse transit time), our method effectively uses one device and an initial calibration and obtains comparable BP results [105,106].

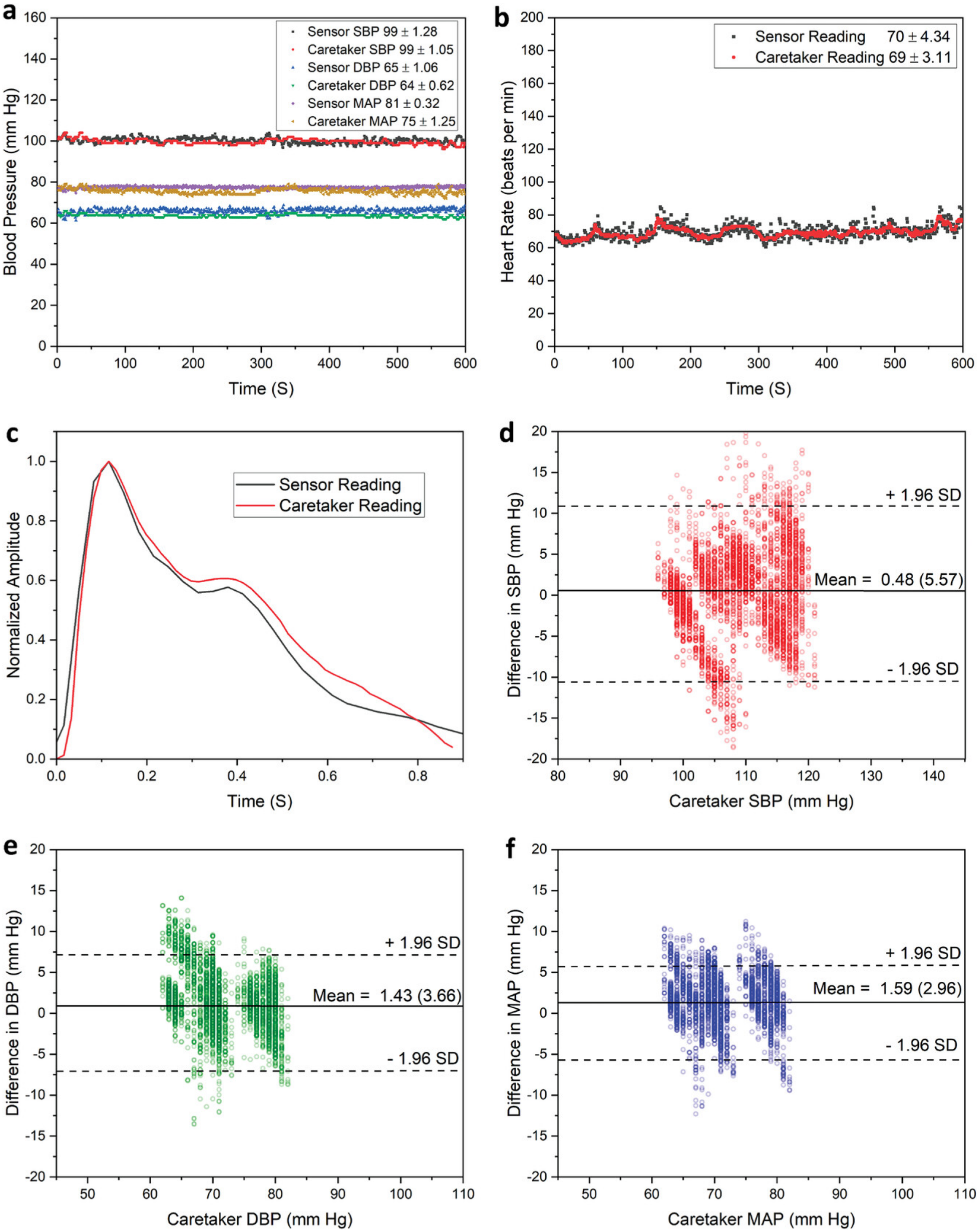

Figure 10. Result comparison between the Caretaker and the sensor. (a) Tracking of systolic, diastolic, mean arterial pressure, and (b) heart rates from both devices for one subject. (d) A pulse alignment example for waveform similarity analysis. The Bland-Altman analyses for (d) systolic blood pressures, (e) diastolic pressures, and (f) mean arterial pressures obtained from both devices.

3.4.3: Blood Pressure Waveforms from Different Body Locations

Given its ultra-sensitivity, the sensor could be adhered to the skin with reduced applanation pressure and still operate. The reduced applanation pressure encourages the sensor to be worn for long term. To verify, the sensor was placed above the temporal, carotid, radial, and dorsalis pedis with the help of a piece of scotch tape (**Figure** 11). The results demonstrated that good waveforms could still be captured under significantly reduced pressure. According to the calculation, approximately 0.55 kPa pressure was exerted by the tape, one-fortieth of that from the applanator.

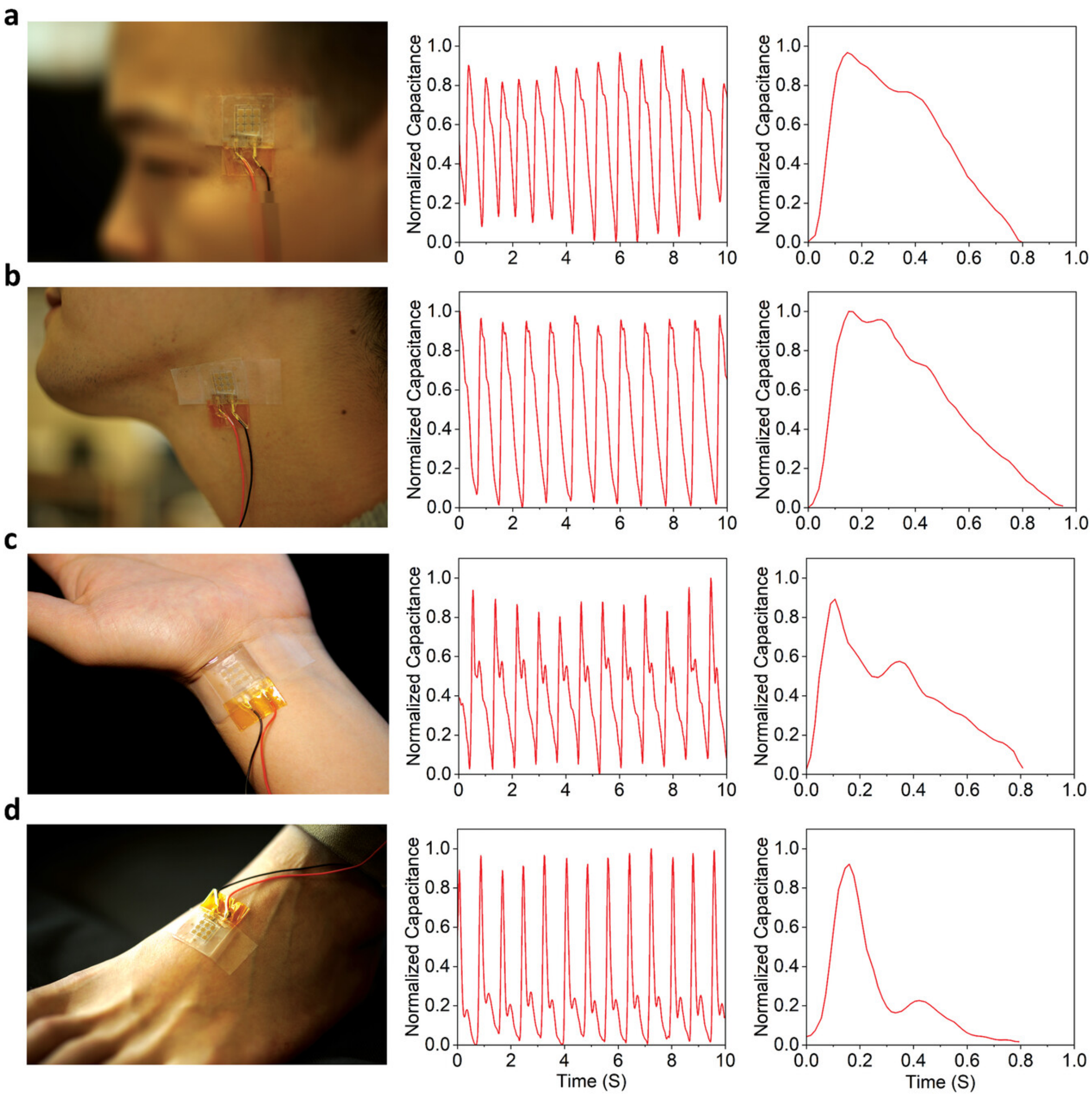

Figure 11. Sensor placement on different superficial arteries and their respective waveform. The sensor is placed on the following locations and obtained their respective waveforms: (a) Temporal artery. (b) Carotid artery. (c) Radial artery. (d) Dorsalis pedis artery.

3.5: Conclusion and Future Prospects

In conclusion, an ultra-sensitive sensor was demonstrated to be capable of capturing continuous pulsatile waveform despite the absence of an applanator. With the help of iontronic dielectric and air gaps, the new sensor design had extreme sensitivity, high baseline capacitance, and a big dynamic range. The use of daisy-chain-shaped electrodes ensured the sensor had easy and fast alignment with the artery. All the advantages above allowed the new sensor to take accurate and continuous BP values using one initial calibration.

However, despite innovations associated with this sensor, many improvements are still needed. More subjects should be recruited for the validation of the sensor, and perhaps the A-line should be used for the ground truth for those subjects. Compared to the Caretaker, the A-line should provide more accurate blood pressure values that can help our sensor better gauge its measurement accuracy and, subsequently, make proper design adjustments. In addition, the A-line can also avoid the Caretaker's inability to tolerate movement and big changes in HR. To further verify the sensor's ability to detect abnormalities in blood pressure, subjects with certain known medical conditions should also be recruited so that this sensor's efficacy in detecting various conditions can be proved.

Using the data collected from the sensor and those from the better ground truth, a better calibration method can potentially be developed so that the blood pressure waveforms can be converted to beat-to-beat blood pressures more accurately. A good method will be using certain machine learning methods to extract features from the waveforms and find their correlations with the corresponding values from the ground truth. The data collected can be used for training and testing the accuracy of the machine learning model.

CHAPTER 4: LC-based Sensor for Congestive Heart Failure Monitoring

4.1: Background and Motivation

Another category of cardiovascular diseases is heart diseases, and it typically leads to heart failure (HF). HF is affecting roughly 7,000,000 people in the US, causing 700,000 deaths annually [107]. Under the influence of HF, the failing heart cannot supply sufficient cardiac output for regular metabolic activity or accommodate enough venous return [108,109]. After initial diagnosis and treatment, about 25% of the patients need hospital readmission after thirty days [110]. According to research, 34.6% of the patients experienced 30-day hospital readmission, and the one-year death rate was as high as 30% from 2015 to 2019 [111,112]. This death rate and readmission are high since HF severity progresses over time and eventually becomes congestive heart failure (CHF) if left uncontrolled, and there is no cure known for the end stage of HF. Eventually, fluid builds up in some organs and lower bodies, resulting in complications in kidneys and dysfunction in other organs [108,109]. The fluid buildup is typically observed on the patient's foot, and the symptom is called edema (**Figure** 12). When a patient is experiencing heart failure, his/her heart will be too weak to pump blood, and that encourages blood accumulation in the blood vessels. Blood accumulation leads to increased hydrostatic pressure that promotes the fluid to leak from the vessel into the interstitium. The same fluid buildup mechanism is also applicable to other organs.

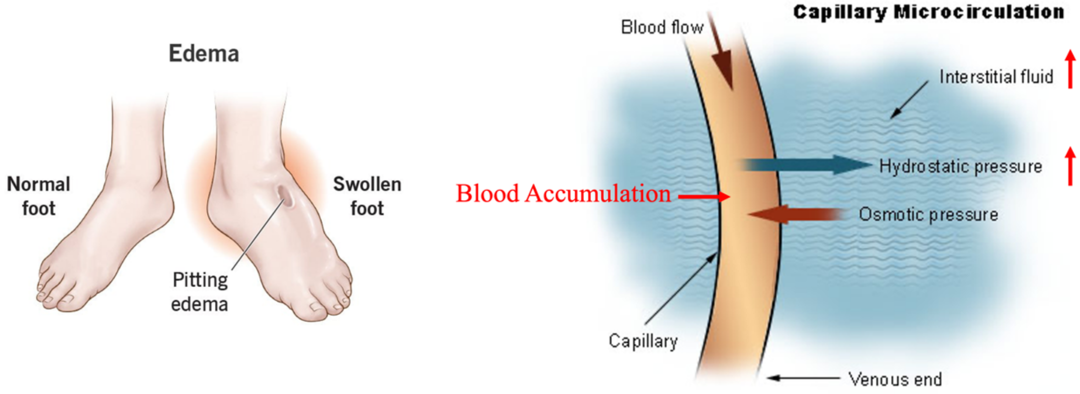

Figure 12. The edema symptom and its cause.

The high readmission and death rates are largely due to the lack of early diagnostic methods [113,114]. As such, it is important to detect the decompensation as early as possible since delays in medical intervention cause further complications and severity, incurring prolonged hospitalization time and increased healthcare costs [115–118]. However, CHF tracking is still based on patient-reported symptoms that are subjective observations [119]. Therefore, an alert method that provides early and pre-symptomatic signs is needed. Many other methods are available in clinical settings, but they are not convenient for continuous monitoring at home [21–26].

Blood pressure is one of the potential biomarkers for CHF, but its continuous trends are needed for CHF prediction [120,121]. The arterial line is the most accurate method for such a purpose, and its operation involves the insertion of a catheter into the artery for direct pressure sensing [122]. The Chronicle and the HeartPOD are the two products inspired by the arterial line since they both require catheter insertion into the ventricle or atrium for direct blood pressure measurement[27,123–125]. However, these devices have large form factors due to the presence of power supplies and information communication software. In contrast to implanted catheter-based devices, CardioMEMS is a small device that is implanted in the pulmonary artery, and it senses the BP inside [27,28]. However, CardioMEMS tends to bond with the vessel wall and therefore, becomes hard to extract without damaging the interior of the artery[126]. In addition, it is hard to install and costly.

Interstitial fluid pressure (IFP) is a potential biomarker for CHF tracking, but it is typically overlooked [107]. In the process of congestive heart failure, the ventricles fail to pump enough blood into the body, and blood accumulates in the veins, contributing to elevated venous pressure [127–129]. Consequently, elevated pressures in veins cause elevated hydrostatic pressures in capillaries, resulting in the leakage of fluid and electrolytes into the interstitium [129]. When the leakage rate exceeds the lymphatic system's draining capacity, fluid will remain in vascular space, and IFP will increase [127]. Usually, a 7 mmHg increase in IFP is expected before CHF patients can see observable edema (**Figure** 13a) [130–132]. Although a positive relationship exists between IFP and edema, and some sensors can track edema via swell monitoring, observable edema already indicates an abnormally high IFP value[133–139]. It is said that the heart's pumping ability has already decreased to 1/3 of its normal value when observable edema is seen [130,131]. As such, continuous monitoring of IFP can give a more direct and earlier decompensation sign than monitoring of observable edema.

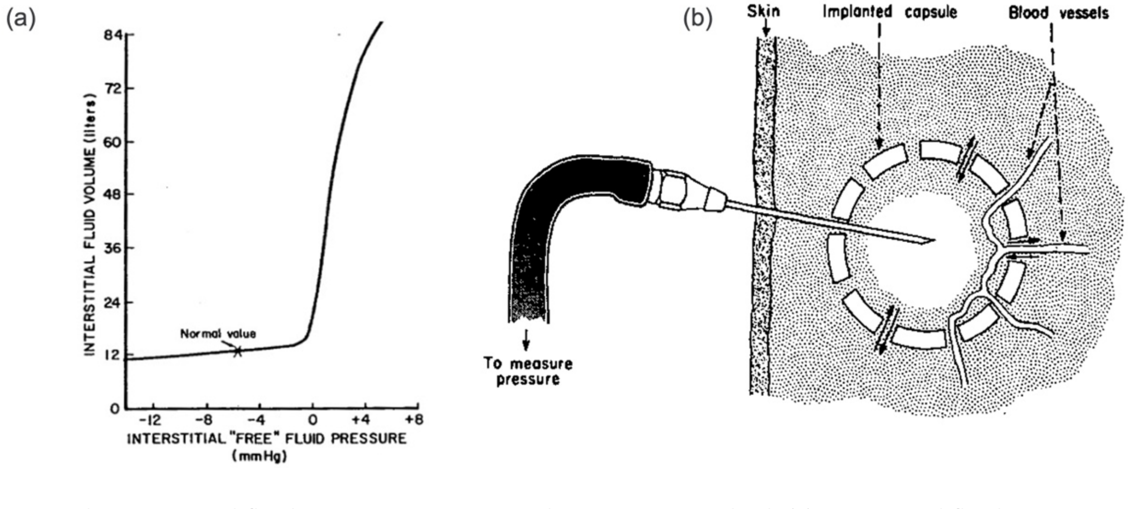

Figure 13. The interstitial fluid pressure increase and its sensing method. (a) Interstitial fluid pressure increases when fluid builds up. (b) The traditional method of measuring interstitial fluid pressure[130–132].

Currently, IFP is measured via inserting a catheter into a porous sphere, but this method is invasive, and complications can occur in the long term (**Figure** 13b) [130–132] [132,140–146]. Hence, it is not ideal for continuous monitoring and, thus, not useful for CHF prediction.

Miniaturized pressure sensors are ideal candidates since their small size allows minimally invasive implantation, a surgery that allows the sensor to monitor IFP directly. Compared to those catheter-based devices, implanting device subcutaneously is much easier. Nevertheless, some sensing methods are more suited for this specific purpose. Piezoresistive and optical sensors need power supplies to operate [142,147–150]. Battery size and life also contribute to their impracticality. Piezoelectric sensors can operate without any power supply, but they are best at obtaining dynamic pressure changes, not IFP, which slowly increases [151]. Capacitive pressure sensors are ideal not only for their simple design but also for their easy integration with inductors to form LC-type pressure sensors that can operate wirelessly without any power supply[152–172]. The resonant frequency of an LC-type sensor is quantified by the following:

$$f = \frac{1}{2\pi\sqrt{LC}}$$

where L stands for inductance, C stands for capacitance, and f stands for the resonant frequency of the sensor. When the sensor is experiencing pressure, both C and L will increase, resulting in a left shift in f [166]. This shift is detectable by a readout coil and therefore, allows the detection of pressure changes wirelessly (**Figure** 14).

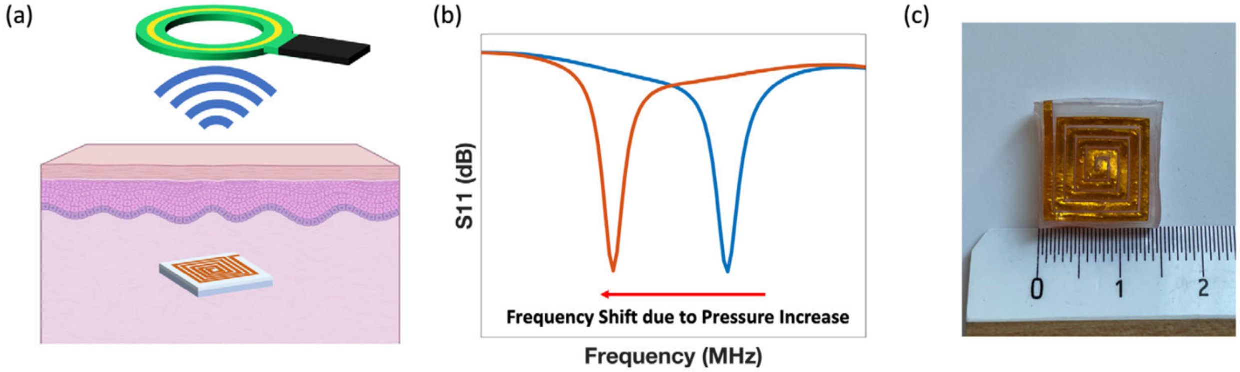

Figure 14. The sensing scheme and picture of LC-type sensor. (a) The sensor's working mechanism: the subcutaneously implanted sensor transmits pressure information to an external coil. (b) Left shift of resonant frequency because of change in pressure. (c) Sensor pictorial demonstration.

In this chapter, an LC-type sensor is introduced for tracking IFP. The top and bottom coils are asymmetrical to each other to realize bigger changes in resonant frequency [166,167]. The sensor contains two copper coils that are carved out from copper foil, and their shapes are defined using a craft cutter on Kapton tape pasted on a PMDS substrate. The planar coils are folded so that one coil is on the top and the other one is on the bottom. An Ecoflex layer (3 mm thick) is placed between them as their separation layer. The sensor is suited for inexpensive batch production due to its simple design, fabrication steps, and materials. Its sensitivity is as high as -3.11 MHz/mmHg due to the use of soft Ecoflex as the dielectric material. Its form factor is acceptable for an implant, and the sensor can transmit pressure information to an external coil despite being separated by pork skins (4 layers, 12.7 mm thick in total). An in vivo IFP was also simulated where the sensors were inserted between pork skins and showed an even higher sensitivity of -8.03 MHz/mmHg.

4.2: Sensor Overview and Fabrication

4.2.1: Sensor Fabrication

A piece of copper foil was pasted on a piece of double-sided Kapton tape, and they were mounted on a piece of PDMS sheet. The coils were carved using a craft cutter named the Silhouette Cameo 4 system. The gaps between the coil turns were kept at 0.25 mm for all coils since this length was the resolution limit of the craft cutter. The craft cutter's force and speed were set to be 12 and 4, respectively. The cut depth into the substrates was set to 2 (about 0.2 mm). All these craft cutter settings ensured the blade could cut through everything but not the PDMS sheet. The substrate was folded after oxygen plasma treatment and boned with Ecoflex dielectric. The detailed fabrication flow is shown in **Figure** 15.

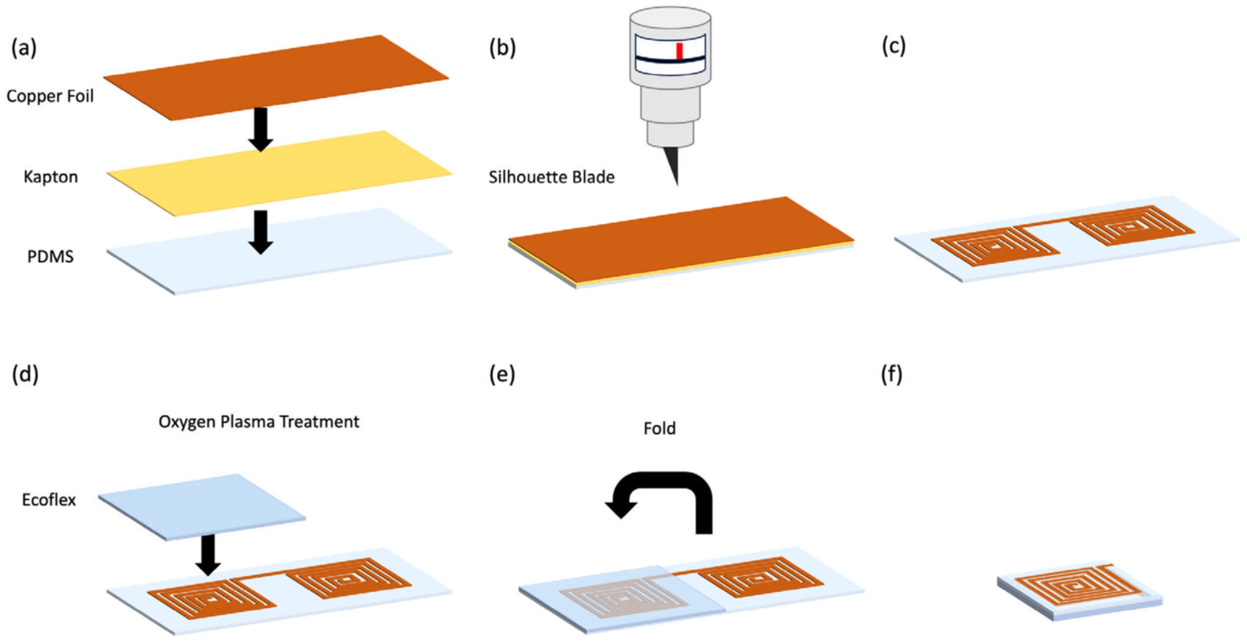

Figure 15. Fabrication flow of the LC-type sensor. (a)Assembly of different layers. (b) Carving foil into desired shapes. (c) The planar coil after carving. (d) Ecoflex dielectric layer assembly after oxygen plasma. (e) Substrate folding. (f) The assembled sensor.

4.2.1: Sensor Selection Process

Sensors with different form factors were made according to the fabrication flow explained in **Figure** 15, and they were tested to determine the smallest possible sensor that can communicate across the body tissue. Sensor designs with different turn numbers and turn widths were fabricated, and the same readout coil was used to interrogate the resonant frequency of the sensors. The readout coil itself had self-resonance peaks that were visible in the frequency spectra. These peaks could overlap with the sensors' resonant frequency peak, making shift detection more challenging[173–175]. Beyond 800 MHz, the readout coil had obvious background peaks (**Figure** 16a). The sensor should have a resonant frequency less than 800 MHz so that it would not overlap with the peaks in the background. In addition, sensors with high MHz resonant frequencies will have shallow tissue penetration depth after being implanted and therefore, will have suboptimal coupling with the readout coil. Hence, only sensors with resonant frequencies below 800 MHz were taken into consideration[176] (**Figure** 16b).

The rest of the sensors were further checked to see if they could communicate with readout coil cross pork skins. Resonant frequency peak (S11) heights were recorded when separated by different layers of pork skin. At higher separation distances, sensors whose coil widths were 0.5 mm could not have detectable peaks. Their narrow coil widths led to high coil resistances, causing high energy dissipation and low energy reflection to the readout coil. When the separation distance was increased, less energy was delivered to the readout coil, and hence, the S11 peak finally disappeared. Amongst all the remaining sensors, the sensor shown in **Figure** 16d was chosen since it had the smallest form factor and yet, could communicate with the readout coil across four layers of pork skin (12.7 mm thick in total). Edema usually appears in lower limbs first, and the average subcutaneous tissue thickness in legs is 10.79 mm for males and 12.44 mm for females [177]. As such, the experiment demonstrated that the sensor could communicate with an external coil even after implantation.

The sensor's durability was also demonstrated by performing a fatigue test. The connection that joined two coils was cut in the middle so that each coil behaves as one of the capacitor plates. During the fatigue test, the change in capacitance could be monitored using an LCR meter. The sensor was compressed by 50 kPa of pressure for 2500 cycles (**Figure** 16e and f). In each loading cycle, the change in slope was seen since the dielectric gradually became incompressible when pressure was loaded. In each unloading cycle, the Ecoflex layer experienced slow relaxation when the pressure was unloaded. No obvious amplitude changes or baseline wandering was seen, showing the sensor could endure repeated mechanical distortion and still offer reliable signals.

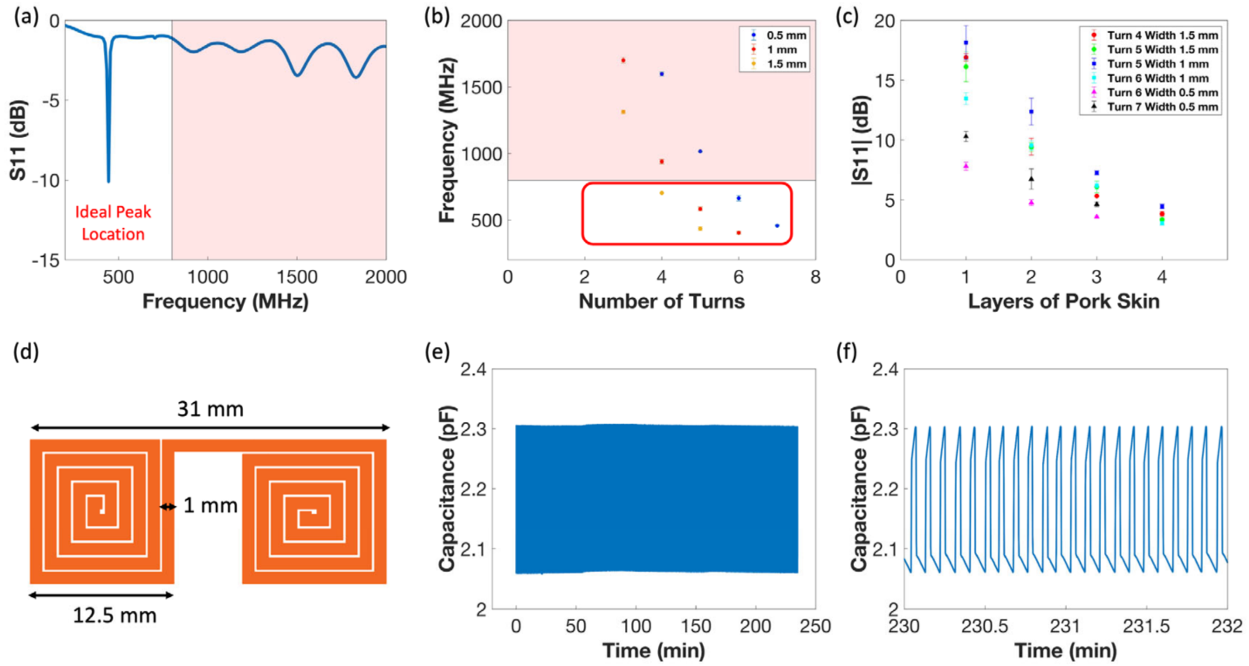

Figure 16. LC-type sensor choosing process, detailed design, and cyclic test. (a) Readout coil's spectra background and an ideal peak location example that is below 800 MHz. (b) Different designs' resonant frequencies. (c) S11 peak heights at various separation distances. Error bars are standard errors. (d) The final sensor form factor. (e) Sensor capacitance change during fatigue test. (f) Fatigue test waveform.

4.2.2: Sensor Characterization

For sensitivity comparison, three dielectric materials were chosen and tested as the dielectric material. They were Ecoflex, PDMS, and sponge. The purpose of the sponge was to provide an isolation layer that prevented the coils from touching each other. Normal pressures were applied to the sensors, and corresponding changes in resonant frequency were recorded. When Ecoflex was used as dielectric material, the sensors showed an average sensitivity of -3.11 MHz/mmHg in the low-pressure range. The sensitivity was decreased to -0.104 MHz/mmHg in the high-pressure range since Ecoflex was harder to compress (**Figure** 17a). Compared to sensors that used the other two dielectric materials, the sensor that used Ecoflex had higher sensitivity since Ecoflex had a higher dielectric constant than sponge and softer mechanical properties than PDMS. A representative frequency shift under different pressures is shown in **Figure** 17b, demonstrating the sensor had high sensitivity in the low-pressure range. The asymmetrical coil layout contributed to the high sensitivity since pressure compressed the two copper coils and brought them closer to each other, increasing the capacitance and the inductance (due to mutual coupling) of the two coils. Both encouraged a more significant frequency shift. Other works used similar structures and achieved desired results as well [165–167].

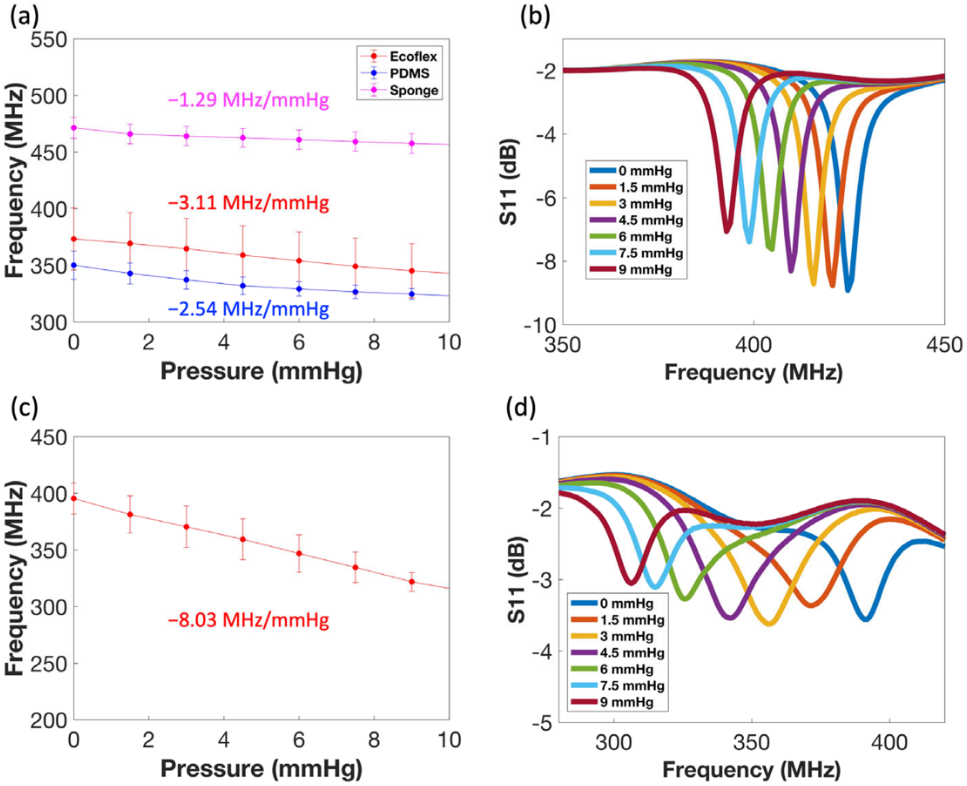

Figure 17. LC-type Sensor sensitivity in a normal environment and sandwiched between pork skins. (a) Averaged sensor sensitivity and (b) frequency shift at low-pressure range. (c) Averaged sensor sensitivity and (d) frequency shift at low-pressure range when inserted between pork skins. Error bars are standard errors.

4.2.3: Sensor Pseudo In Vivo Testing

To verify their ability to capture pressure change as implants, the sensors were inserted between pork skins, and the same pressures were applied again. The corresponding frequency shift was captured as well. The presence of water in the pork skins effectively increased the dielectric constant around the sensor and hence, increased its capacitance too. As a result, the sensors' average sensitivity increased to -8.03 MHz/mmHg (**Figure** 17c). The corresponding frequency shift under various pressures is shown in **Figure** 17d. Despite the peaks becoming shorter and more distorted, shifts were still seen. The sharpness and height of peaks were determined by the Q-factor, and it is defined by the following equation:

$$Q = \frac{1}{R}\sqrt{\frac{L}{C}}$$

where R is the resistance, L is the inductance, and C is the capacitance, respectively. The presence of water increased the sensor's capacitance, leading to lower Q-factors and shorter peaks with slight distortion. Nevertheless, our sensor still had better sensitivity compared with those of other sensors published in other works[154,158–167,178,179].

4.2.4: Sensor Simulation

To verify the sensor sensitivity, simulations were performed. The field distribution around the sensor was calculated via the finite-difference time-domain (FDTD) method using the discrete port excitation method. A frequency domain solver and tetrahedral mesh were utilized, and boundary conditions in all directions were set to open. In this simulation, the gradual pressure increase on the sensor was set to be equivalent to the small stepwise decrease in dielectric layer thickness due to the model's complexity. A similar approach was also used in previous publications [180]. The decrease in dielectric layer thickness incurred an increase in equivalent inductance and a decrease in resonant frequency. According to the simulation results, the sensor inserted between pork skins had higher sensitivity due to the presence of water. Indeed, water's high dielectric constant led to high capacitance that encouraged the sensor to have enhanced sensitivity (**Figure** 18a and b). The simulation results and experimental results followed the same trend.

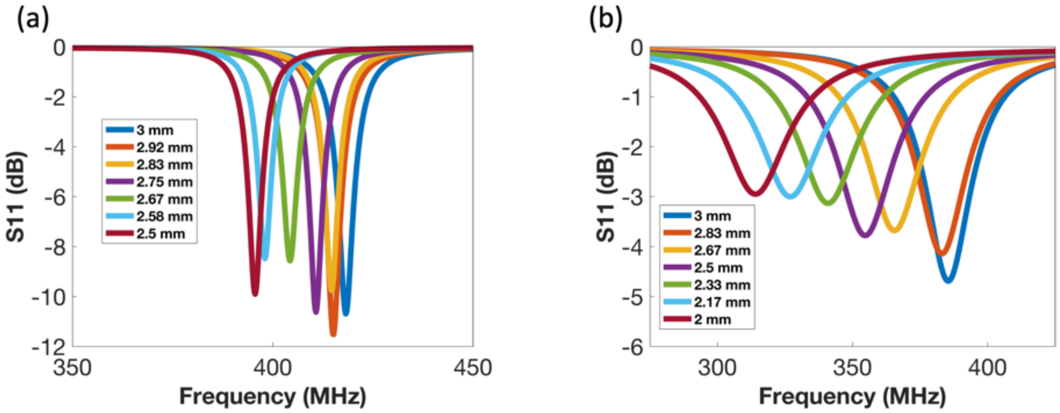

Figure 18. LC-type sensor simulation results. (a) Sensor in a regular environment. (b) Sensor inserted between pork skins.

4.3: Conclusion and Future Prospects

In conclusion, a battery-free and wireless pressure sensor is presented in this work. The sensor has a low profile and can operate without the use of any battery, making it suitable for implant via minimally invasive procedures. The sensor demonstrated high sensitivity and could communicate across body tissue. Hence, it is a suitable device for monitoring changes in IFP and predicting the onset of CHF after implantation.

Despite the sensor's high sensitivity and robust design, a proper encasement should be designed for it (**Figure** 19). The encasement will have a hard silica case so that other mechanical forces will not be able to deform the sensor. One side of the silica membrane will have pores defined by the laser cutter so that interstitial fluid can contact the sensor, and hence, the silica encasement will allow selective sensing of the fluid pressure. To minimize the stiffness mismatch between the body tissue and silica, the silica encasement will also be coated with silicone. These two materials were used for encasing the CardioMEMS too.

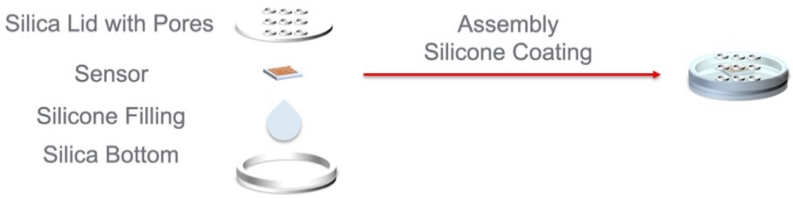

Figure 19. The final sensor design with proper encasement.

CHAPTER 5: Strongly Coupled Magnetic Resonators for Joint Angle Monitoring

5.1: Background and Motivation

Tracking human movements smoothly and continuously is important for many fields, including but not limited to rehabilitative medicine, sports science, ergonomic study, etc [181–187]. Stroke is a type of cardiovascular disease that can lead to paralyzed body parts, and regaining the ability to move is a significant part of rehabilitation for stroke patients. Their joints' ranges of motion are good metrics for their rehabilitation. Current methods for joint movement monitoring have their respective benefits and drawbacks. Nonwearable methods like those that utilize optical cameras, regardless of whether retroreflective markers are involved, are limited to environments with clear lines of sight[188–191]. Those electromagnetic methods can identify physical activity from far away, but they are best used indoors and most capable of activity classification, not detailed motion analysis (bending or rotating).

Wearable devices offer many potential monitoring methods. Time-of-flight technologies that use ultrawideband or ultrasonic signals measure signal travel time. However, they are limited by their bulky sizes and are prone to cause injury[192]. Those inertial measurement units provide users with good degrees of freedom and comfort, but those devices often experience sensor drift and consume lots of power[193]. Some sensors are placed across joints to detect strain-induced resistance change, but they limit user movement and tend to have short operational life due to repeated wear[194,195]. Their durability and device flexibility are also limited due to the use of microelectronics with soldered connections.

Smart textiles offer users integrated and user-friendly device opportunities[196–199]. The most promising innovation amongst smart textiles is the use of strongly coupled magnetic resonance between wearable inductors[200]. The idea of this type of application stems from serving as passive sensor nodes that enable wireless power transmission[199,201–206]. One of the approaches for joint angle monitoring is through measuring wireless power transfer efficiency[207,208]. In this approach, loop antennas are placed longitudinally along the joint, alleviating the problems from lateral placement across the joint. In this chapter, a pair of strongly coupled magnetic resonators is proposed for joint angle monitoring. In this approach, the coupling coefficient and reflection are related at the reader port, reducing the number of ports to only one. Its operating principle is based on Faraday's law of induction. Two strongly coupled resonators alter their respective resonant frequencies due to mutual energy exchange, causing the creation of two new frequencies[209–211]. One of the frequencies is higher, and the other one is lower than the original one. Both of them can be captured by reader port in return loss. These coils can be mounted onto clothes and skin and operate without any battery. The system will need a wearable mini vector network analyzer, replacing the need for bulky equipment. This approach uses adaptable magneto-inductive loops that are positioned on two sides of a joint, leaving the range of motion unrestricted and minimizing mechanical failure due to repeated flexing. The loops used in this approach are made to be flexible and planar, keeping stable spectral behavior close to the human body with an integrated lumped capacitor to balance the skin's stray capacitance. Initial angle calibration was performed before the tests on the human body. A rule-based method based on measured angles was used to classify various movements.

5.2: Sensor Overview and Fabrication

5.2.1: Overview and Principle

Figure 20a demonstrates the placement of two strongly coupled resonators and reader antenna across a joint with a certain separation distance. The upper arm rotates about the center of the joint to achieve flexion. When fully extended, the arms are straight, and the flexion angle is 180 degrees. The flexion angle decreases as the forearm flexes about the joint. The forearm can also rotate about the joint. Under both scenarios, the two loops are misaligned, causing changes in the coupling coefficient. The changes in the coupling coefficient can be used to calculate the changes in flexion and rotation angles.

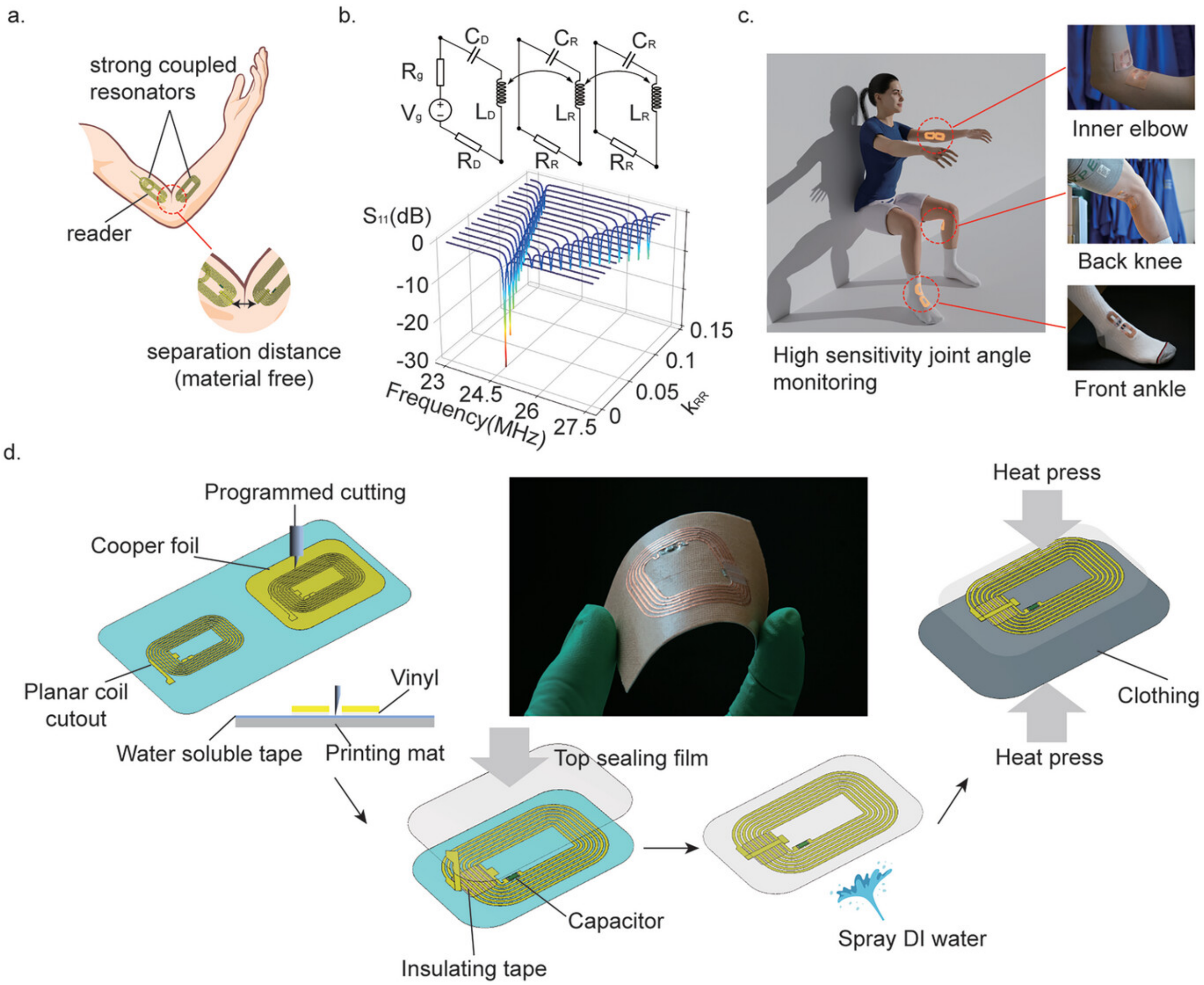

Figure 20. Sensor demonstration, simulation, and fabrication. (a) Sensing mechanism. (b) Equivalent circuit diagram of the strongly coupled resonator and the resulting resonance split. (c) Same setup for other joints. (d) Sensor fabrication and integration on cloth.

Figure 20b is showing the layout of each magnetically strongly coupled resonators that have multiple loops that have a self-inductance of L, an effective ohmic resistance R containing self-resistance and fringing currents due to background loss media. The resonance properties of the loop are determined by the effective capacitance, consisting of structural stray and discrete tuning component of capacitance C. A lumped surface mount capacitor is incorporated to minimize the effect of stray capacitance and achieve resonant responses that are not affected by skin proximity.

The resonance characteristics of a circuit with coupled inductors are obtained through Kirchhoff's voltage law, and the equation is differentiated with respect to time to remove the integral term. Assuming no damping and only care for the resonant frequencies. For each loop, its behavior is defined by the following equation:

$$L_R \frac{d^2 I}{dt^2} + \frac{1}{C_R} I + M_{RR} \frac{d^2 I}{dt^2} = 0$$

Assuming the current I in resonators has sinusoidal time dependency with frequency w. The solution describing the current will be $I = Ae^{iwt}$. The determinant of the coefficient matrix should be zero to find the nontrivial solution of A:

$$\begin{vmatrix} -w^2 L_R + \dfrac{1}{C_R} & -w^2 M \\ -w^2 M & -w^2 L_R + \dfrac{1}{C_R} \end{vmatrix}$$

Which is derived to be the following equation:

$$w^4 (L_R^2 - M_{RR}^2) - w^2 \frac{2L_R}{C_R} + \frac{1}{C_R^2} = 0$$

Solving this equation will obtain w^2, the squared angular frequencies of the system. The frequency split is due to the mutual inductance M_{RR}. Resistance in the circuit causes energy dissipation that affects the amplitude and the phase of the oscillation, including the resonant frequencies, to some extent. The same setup can also be used on knee and ankle joints (**Figure** 20c).

5.2.2: Sensor Fabrication

The loop coil is carved out of copper using a craft cutter (**Figure** 20d). After being tuned by a capacitor and soldered flipped the copper trace, the layers are first stacked from the top, sprayed with water to remove the bottom holder layer, and integrated onto clothes via heat pressing. The loop size is 31 mm in width and 48.4 in length. Smaller loops will have weaker coupling, and the resonators will fail to detect large angles. Bigger loops will be impractical to fit onto clothing and start to impede motion.

5.2.3: Sensor Simulation and Calibration

The strongly coupled resonator’s potential as a joint monitoring device is validated in a benchtop setting using the setup shown in **Figure** 21a. The resonator on the right is kept unbent, bent horizontally, or bent vertically to imitate sensor deformation when attached to actual joints. Simulated magnetic fields at a 30-degree flexion angle are presented in **Figure** 21b. As the two coils are brought closer to each other, a stronger magnetic field is noticed. The enhanced field causes stronger mutual coupling and, subsequently, makes the resonant frequencies split wider (**Figure** 21c). For instance, when the top resonator is vertically bent, the frequency split is larger because the middle of the loop is closer to the other loop. As such, the initial deformation of the loop might have practical implications for different joints, which have their respective curvature that modulate the initial deformation of the resonators. The initial curvature will modulate how this inductor interacts with the other loop, specifically on changing how resonant frequency split and how much frequency split changes when the joint flexes. **Figure** 21d shows the simulated results and experimental results for all three curvature conditions. A protractor is used to modulate the angles between the coils so that frequency splits can be obtained at different angles. When the loops are brought close to each other, there are higher deviations between the experiment and simulation, possibly due to our inability to obtain the same angle and the loop’s high sensitivity at low angles.

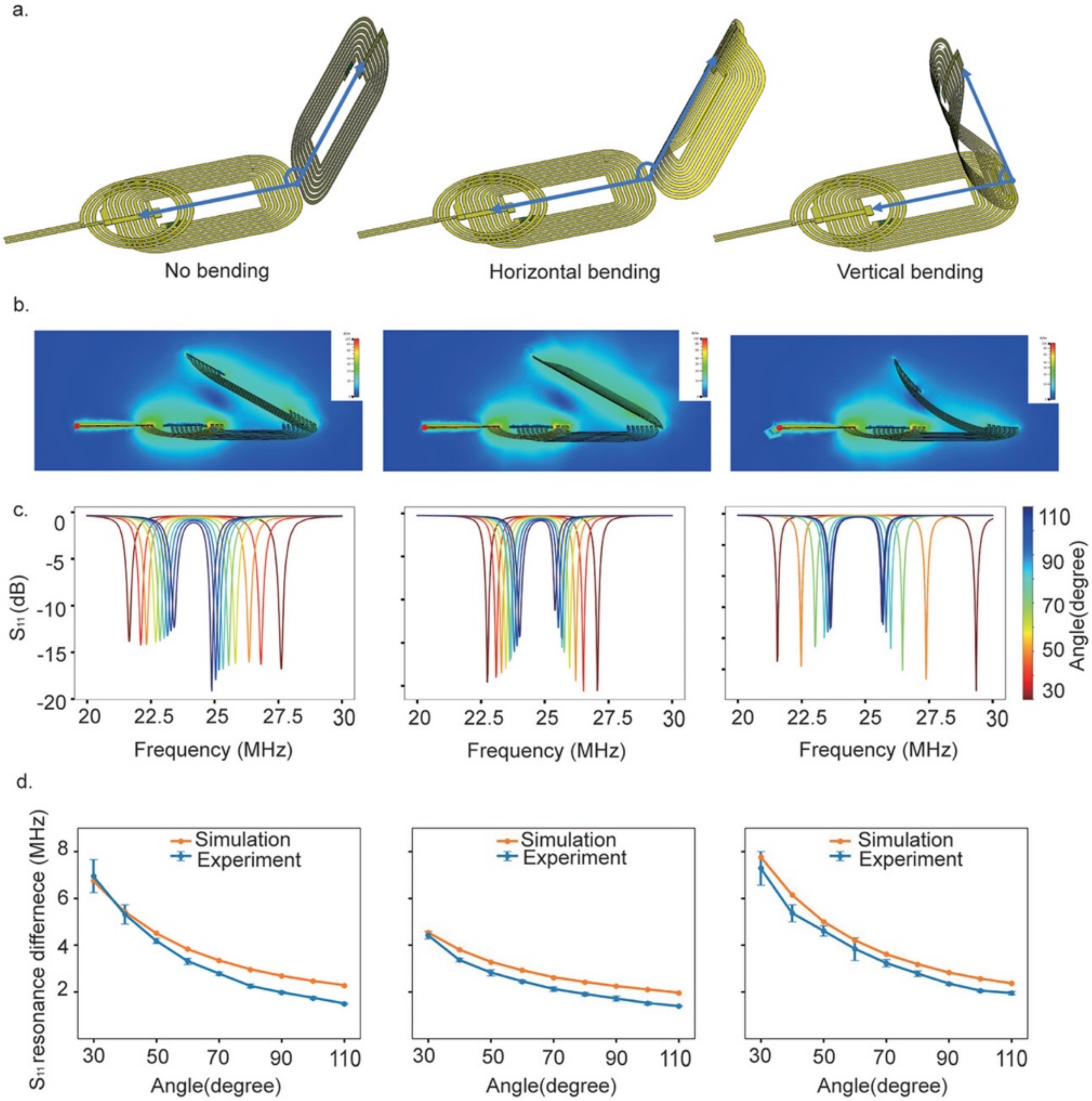

Figure 21. Sensor performance simulation and benchtop test. (a) Sensor at different initial bending states. (b) Magnetic fields obtained from simulation at different initial bending states. (c)Simulated spectra at different bending angles for each initial bending state. (d) Simulated and experimental sensitivities for each initial bending state.

5.3.1: Sensor Performance on the Human Body

MediaPipe is an open-source framework produced by Google and it uses machine learning solution to process video data. In this case, MediaPipe is used to extract joint angles and associate those angles to their corresponding frequency splits so that calibration curves can be made. Loop pairs were used to track the movement of the elbow, ankle, and knee (**Figure** 22). **Figure** 22a and b show the attachment of loops on the forearm and upper arm to measure elbow rotation and bending. S11 values were recorded for every 45-degree increment for rotation and every 10-degree increment for bending. Rotation has higher sensitivity since it generates high loop distances and therefore, encourages higher frequency split changes. Similarly, the same setup was adopted for the ankle and knee (**Figure** 22c and d). Joints were held at different bending angles, and the corresponding frequency splits were recorded. All measurements were conducted three times so that means and standard deviations could be obtained.

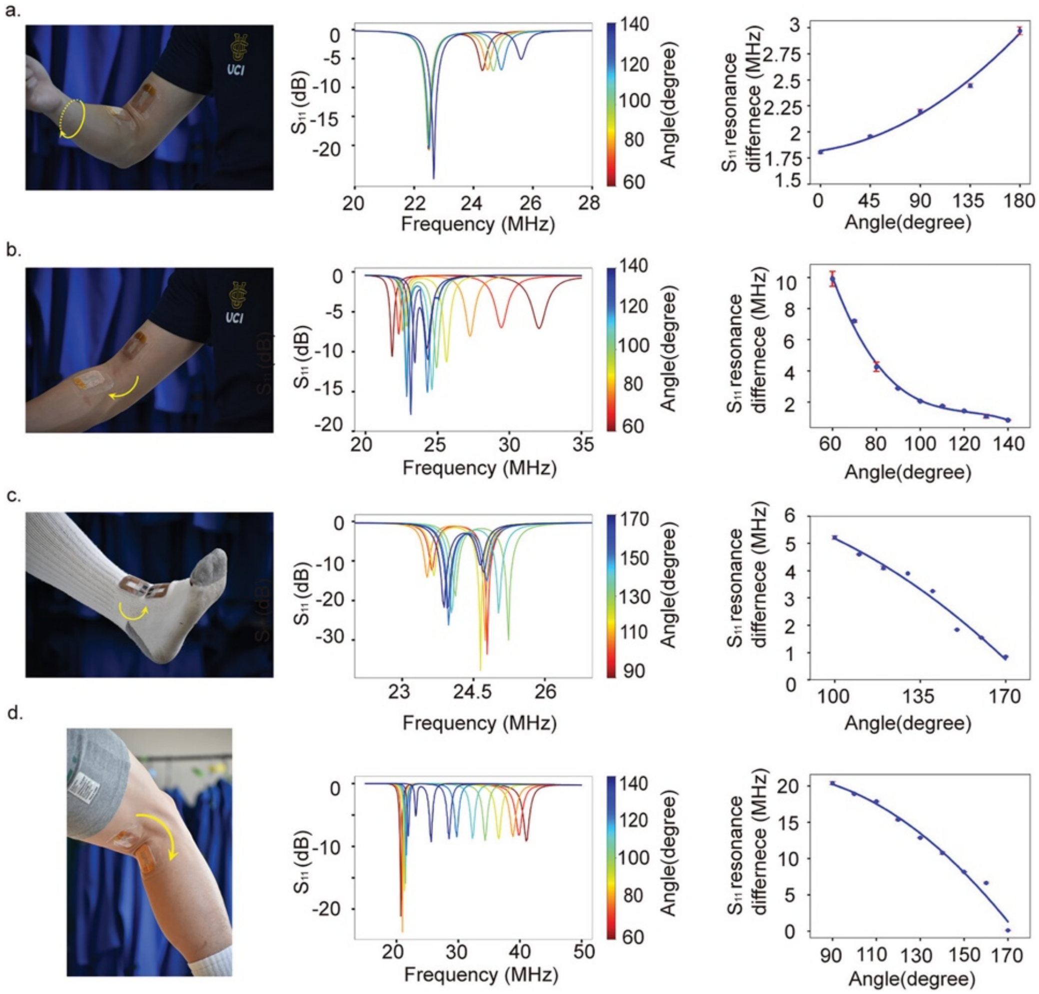

Figure 22. Sensor performances at different joints. (a) Sensor performance on the elbow for rotation measurement. (b) Sensor performance on the elbow for bending measurement. (c) Sensor performance on the ankle for bending measurement. (d) Sensor performance on the knee for bending measurement

5.3.2: Sensor Fatigues Test

A fatigue test was performed to verify the stability and reliability of measurements. One of the loops was fixed on a test stand force gauge, and the other loop was fixed below. The force gauge could perform vertical and periodical movement so that dynamic variation in coupling coefficient could be mimicked during joint movements. The performances were measured at three different movement speeds, and 1200 cycles were performed at each speed. Highly repeatable signal changes were obtained from this benchtop setting since our sensing scheme decouples sensor output from sensor strains (different from strain-based sensors).

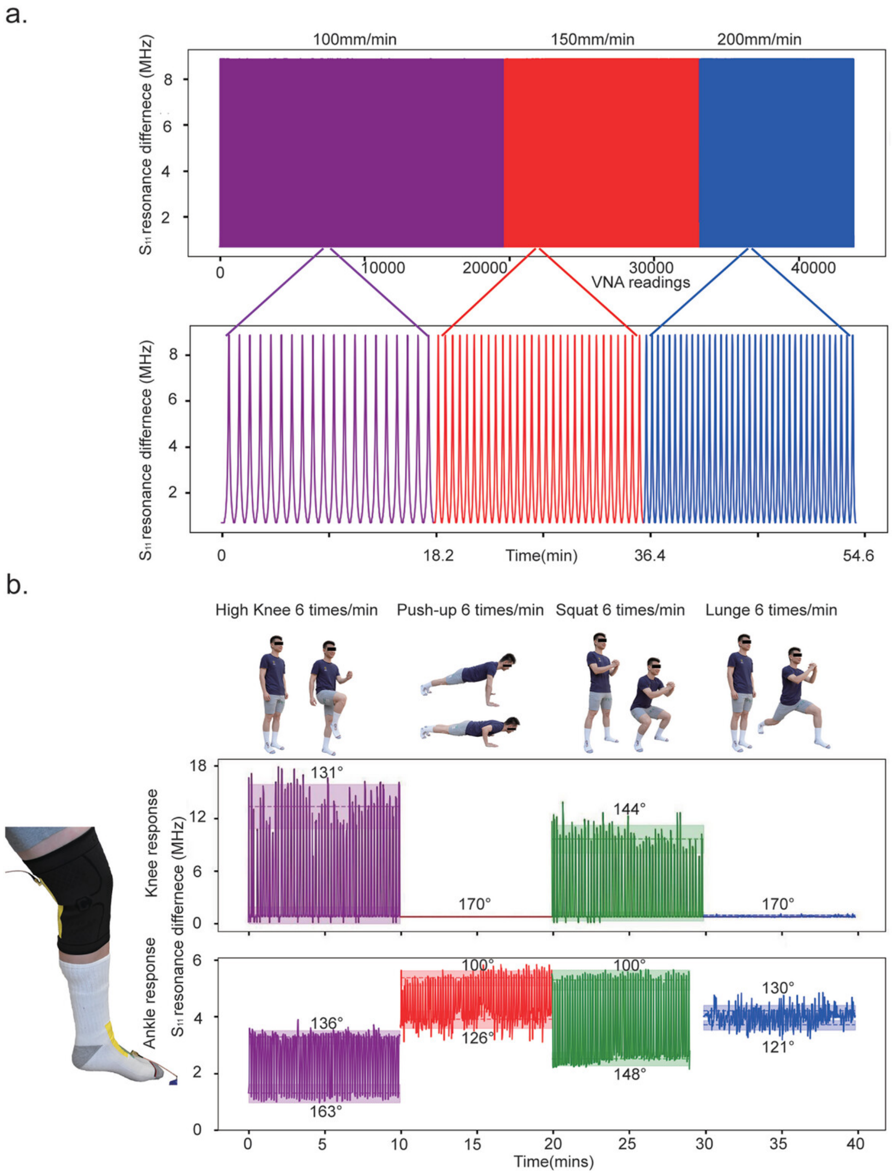

Figure 23. Fatigue test and body joint monitoring networks. (a) Fatigues test of the loop pairs and the dynamic spectral response at three different speeds. (b) Simultaneous monitoring of knee and ankle joints during different exercises.

5.3.3: Network Formation for Simultaneous Knee and Ankle Joint Monitoring

Different physical exercises were performed while the subject was wearing the loop pairs. The subject put on the socks and knee braces with integrated loop pairs, realizing a joint monitoring network along the leg. The subjects were asked to perform a set of exercises, including high knees, push-ups, squats, and lunges. The initial and final positions for each exercise and their respective signal changes are shown in **Figure** 23b. A miniVNA and a readout coil were used as the detection unit, and the coil was fixed to the body inductor coils. Obviously, high knee and squat require big movement in both the knee and ankle, and therefore, significant frequency splits were observed for both coil pairs. For push-ups and lunges, the knee joints were not significantly bending, and the ankle joint only experienced slight bending. As such, negligible frequency splits were seen on the knee joint, and only slight frequency splits were observed on the ankle joint.

Given the different types of frequency split seen on each loop pair during different exercises, this joint monitoring scheme can be used to recognize different types of activities. Admittedly, variabilities in frequency splits are seen in each type of exercise due to the imperfection in natural motions. The interquartile range was used to exclude the abnormal data and determine the boundary range. The centroid values of frequency splits were calculated for each exercise and used for specific angle calculation via a rule-based method. Using this strategy, frequency splits were associated with their corresponding angles (**Figure** 23b).

5.4: Conclusion and Future Prospects

In this chapter, a universal approach for joint angle monitoring is proposed. This approach uses strongly coupled resonators integrated with textiles and can capture a wide range of movements with high accuracy. Limitations in conventional joint monitoring methods, such as the need for clear line-of-sight, complication setup, and restriction on natural movement, are avoided in this sensing scheme. The robustness of our sensor and its capability to offer real-time joint angles may benefit fields such as rehabilitative medicine, sports science, etc. This sensor is especially important for post-stroke patients since they can continuously monitor joint angle, an important metric to gauge their extent of rehabilitation.

Despite these many innovations, this sensor design still has room for further optimization. Despite the many advantages of those LC sensors, a bulky and ridge VNA device is still needed. The existing VNA is neither wearable nor easy to carry around (**Figure** 24a). When multiple LC pairs were used to form a body network, multiple VNAs were also needed, adding further inconvenience. Ideally, the VNA device should also be wearable and small in size. In addition, one VNA should be able to monitor different LC pairs on the body using different parts of frequency spectra. Different parts of the frequency spectra can be utilized by tuning the inductance and capacitance of the LC pairs.

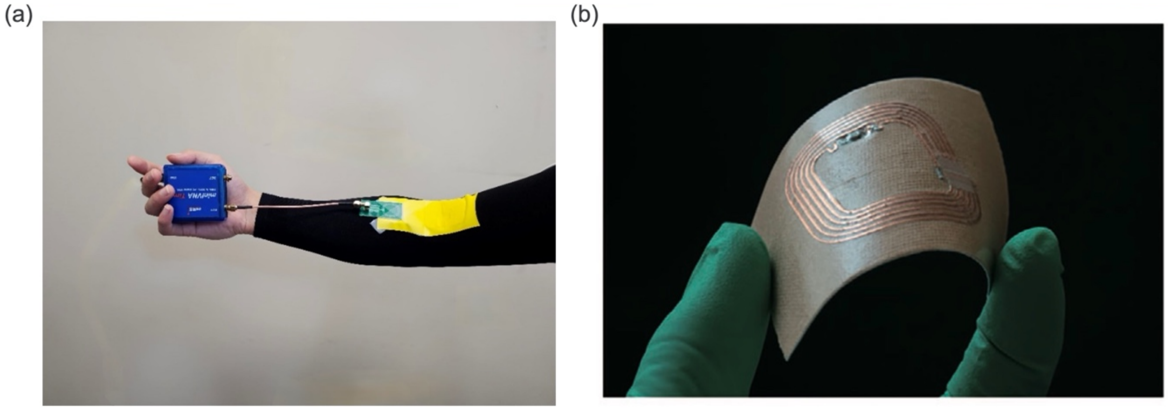

Figure 24. The existing devices used for each LC pair. (a) The bulky VNA. (b) The LC sensor picture.

The existing LC sensor does not have the most optimal wearability due to the choice of materials. The copper foil has stiffness mismatch with the vinyl substrate and can buckle up from the substrate (**Figure** 24b). The copper foil has a certain flexibility, but its flexibility and stretchability are limited, meaning the wearable comfort of the sensor is not optimal. Perhaps the coils can be made with conductive polymers or other conductive materials that not only attach to polymer substrate well but also are soft enough to promote wear comfort.

CHAPTER 6: Limitations of Current Studies and Future Directions

6.1: Challenges Encountered and Limitations of Current Studies

Despite the progress made, many of the problems and limitations remained unresolved in the technologies explained in the above chapters. In addition, many of the designs require further verification on many aspects.

6.1.1: Challenges and Limitations for Blood Pressure Sensors

In **Chapter 3**, an ultra-sensitive capacitive pressure sensor was realized with the help of iontronic dielectric material. The sensor was robust, sensitive, and capable of tracking continuous blood pressure. Despite its many innovations, the sensor and the study both had their limitations. Only a few subjects participated in the experiment, and they were known to be healthy. All the measurements were performed under stationary conditions since the Caretaker is not capable of tolerating movement and needs to be recalibrated when big changes in HR are observed [212]. Due to its soft substrate and ultra-sensitivity, the sensor can pick up many unwanted signals due to body motion and surrounding vibration, imposing difficulties in the processing of the data. Subjects were also told to stay still during data recording since the bandpass filter was only able to process stable data into meaningful blood pressure. Better algorithm designs are needed to make sure the sensor can continuously track blood pressure at any time. Many more clinical trials might be needed to verify that the sensor can be used to identify various conditions. Perhaps machine learning algorithms can be developed using all the subjects' data so that unwanted motion artifacts can be removed, and certain medical conditions can also be detected using the verified model. Finally, the arterial line should ideally be used as the ground truth, and hence, further clinical studies should be pursued for further verification.

6.1.2: Challenges and Limitations for LC-Type Interstitial Fluid Pressure Sensor

In **Chapter 4**, an LC-type sensor was made to monitor interstitial fluid pressure. Despite the promising experimental results, the sensor has not yet been used on any *in vivo* model, and therefore, many of the limitations have not been exposed yet. The sensor was made with an easily accessible tool, but this also limited the minimal feature size achievable. Hence, the sensor can be further miniaturized to become more suitable for implantation using a minimal invasion procedure. Later on, a proper encasement will be designed for the sensor using silica for a hardcover, and silicone will be coated on the silica to minimize stiffness mismatch. The sensor will have pores on one side of the silica case to ensure its direct contact with interstitial fluid.

6.1.3: Challenges and Limitations for Resonator-Based Joint Angle Monitoring Device

In **Chapter 5**, strongly coupled magnetic resonators for joint angle monitoring were made. Despite its many advantages, the coils still impart their stiffness on the substrate. Therefore, clothes with those coils might not be the most comfortable and natural ones to wear. Perhaps alternative materials can be used to make the coils so that their stiffness can be minimized. The readout system was not optimized either since its size was big, and each sensor pair required one readout coil to operate.

6.2: Future Improvements and Directions

If all the shortcomings of the devices mentioned above are addressed in the future, we will have an ecosystem of wearable sensors that focuses on monitoring the entire cardiovascular system. Currently, the entire global population is affected by cardiovascular diseases, and they are already contributing to 1/3 of the global death. The ecosystem for cardiovascular disease monitoring is significant since it has the potential to save those people by providing on-time alerts and treatment.

6.2.1: Future Directions for Blood Pressure Sensors

Our blood pressure sensor can offer continuous monitoring of blood pressure, which indicates the overall vascular system's health and sudden onset of certain detrimental conditions. The band-aid type sensor can capture pulsatile blood pressure waveforms from any pulse points and convert them to beat-to-beat blood pressure. It is not invasive like A-line and avoids the shortcomings of other commercialized devices. A machine learning model can detect conditions based on the features of the waveforms. In fact, an intra-beat biomarker-based algorithm was developed later and used in many of the subsequent clinical studies[213]. The algorithm utilized a wave feature named diastolic transit time to calibrate the blood pressure waveforms to beat-to-beat blood pressure values and the results were better than those obtained from the bandpass filter method used in my publication. Perhaps both diastolic transit time and other wave features could be extracted from waveforms and a neural network-based deep learning algorithm can performed on those features. The algorithm should be able to determine which wave feature have most influence on the blood pressure values and hence, offer better and more accurate prediction.

In addition to those intra-beat biomarkers, the waveforms' temporal dimensions can also provide useful features for blood pressure value calibrations. Two of the most widely accepted continuous blood pressure calibration method are pulse transit time (PTT) and pulse arrival time (PAT). Both methods can be used to calibrate blood pressure since the travel speeds of pulses are proportional to the blood pressure values. PTT utilizes two sensors placed at two peripheral artery sites[106]. PAT utilizes one ECG device, and one sensor placed at a peripheral artery site[214]. Both methods can obtain the pulse travel speed after the synchronization of the two devices. Although our setup utilized only one sensor and a simple bandpass filter calibration method, the resulting blood pressure values are as accurate as those that used PAT and PTT methods. Nevertheless, the incorporation of these temporal dimensions into relevant machine learning algorithms might provide extra insights in the prediction of blood pressure values. The combination of temporal dimension and intra-beat biomarker might be an even better solution than those methods that just rely on one of them[106].

More importantly, more subject with certain known clinical conditions show be recruited for algorithm training and validation purposes. More subjects can provide more waveforms that are useful for the training of the proposed machine learning model. In addition, the recruitment of more subjects might be able to provide more generalizability for the entire population. Those disease-relevant waveform features can also be analyzed so that the model can learn and recognize those features. It will be useful for predicting the onset of those diseases and timely medical treatment can be performed. Some of the clinical studies were already performed. In fact, some wearable blood pressure sensors and algorithms have already been used on post-stroke patients and demonstrate the presence of their unique blood pressure variability[215]. Our sensor design was also approved in neural ICU, and it will be used to capture blood pressure waveform from the carotid artery. The waveforms can be converted to beat-to-beat blood pressure values and they are indicative of intracranial blood pressure because they are obtained from site that is close to the brain. Our sensor design has high sensitivity, meaning it will cause less vasoconstriction since only low applanation pressure is needed. Ultimately, our sensor can replace the invasive method that involves the insertion of a probe into the skull for direct pressure sensing. More similar research should be performed for more clinical efficacy validation.

Aside from the sensors and algorithms, the circuit board system also deserves certain improvement since the current circuit board is rigid and not wearable. Yet, we still rely on rigid circuit boards to process the raw signal and transmit the processed signal. These complex functions can only be achieved using electronic devices made from conventional microfabrication techniques that are mature and capable of achieving small feature sizes. Eventually, the entire circuit should also be wearable for the best user experience and wear comfort. However, there is still a long way to go if we want to develop a fabrication line for wearable circuit boards since different substrates and unconventional materials are used for wearable circuits. Despite the progress in the recent year, microfabrication on wearable substrate is still lacking practicality. In one of the most innovative publications, Zheng et al. presented a method of performing monolithic optical lithography on wearable substrate and stretchable transistor array was produced[216]. However, those transistors were large and approximately 2380 um^2 each. If the same technique is used to reproduce a S9 chip (about 5.6 billion transistors) in apple watch, the chip will be as large as 13 m^2. As such, the current technique is still highly immature and impractical. More innovative methods must be developed to further minimize the feature sizes.

6.2.2: Future Directions for LC-Type Interstitial Fluid Pressure Sensor

Although weaker blood pressure is associated with potential heart failure, it cannot be an absolute indicator of heart failure. Many confounding factors can lead to weak blood pressure, such as anemia, endocrine disorder, and dehydration. As such, blood pressure cannot be a vital sign for a definitive diagnosis of heart failure, and hence, a different biomarker needs to be added to the ecosystem of cardiovascular disease monitoring. It has already been proven that interstitial fluid pressure can serve as an ancillary biomarker, and a practical sensor design was already proposed in this dissertation. When abnormalities in both blood pressure and interstitial fluid pressure are detected, a more definitive diagnosis of heart failure can be decided.

The sensor's promising result so far does not mean it will perform will in actual human body and many additional works need to be performed on the sensor to ensure it will functional well in its intended place. Proper encasement should be implemented on the sensor since the sensor should only sense interstitial fluid pressure. Minimally, a built-in Guyton chamber should be included as part of the proper encasement so that the sensor can selectively sense the fluid pressure, not confounded by other mechanical pressures. In those previous publications, sensors with Guyton built-in chamber were developed to sense the fluid pressure inside of tumors and their encasements were made of relatively soft materials. Although the soft materials have many merits and are frequently used in many wearable electronic, they might not be suitable in this situation since the other mechanical force can also invoke sensor's signal change and confound with the pressure we are interested in. The proposed encasement is demonstrated in **Figure** 19. The sensor will be encased with silica and pores will be defined on one of the membranes so that a built-in Guyton chamber can form. The Guyton chamber will allow the interstitial fluid to leak in so that the change in fluid pressure can be sensed. The hard silica encasement will prevent the sensor from deforming due to other mechanical pressures. Finally, the encasement will be coated with silicone to minimize the potential stiffness mismatch with surrounding body tissue. Both silica and silicone are already widely used in other implantable sensors such as CardioMEMS.

Like the wearable blood pressure sensor, the interstitial fluid pressure sensor also requires a wearable readout system. Currently, a standard VNA was used to characterize the sensor, and VNA was bulky and not portable. The miniVNA used in the joint angle monitoring sensor was more ideal, and perhaps multiple readout coils can be installed to the miniVNA so that not only joint angles but also the interstitial fluid pressure can be measured using the same miniVNA system.

6.2.3: Future Directions for Resonator-Based Joint Angle Monitoring Device

The joint angle monitoring devices are important for the rehabilitation of post-stroke patients since they can gauge their bodies' range of motion. This is an important part of the cardiovascular ecosystem, and its importance in the ecosystem can be further improved by having a miniVNA that has a high sampling frequency. Higher sampling frequency encourages more detailed motion capture and can determine if a subject is doing certain physical activity, a major confounding factor for continuous blood pressure monitoring.

Furthermore, the same magnetic resonator method used in this application might be able to replace the capacitive blood pressure sensor mentioned above. Two LC sensors can be positioned above a pulse point, and frequency splits are used to map out the continuous blood pressure waveform. Perhaps, this sensing modality can be used for capturing blood pressure, interstitial fluid pressure, and motion, and only one miniVNA will be used. Multiple joints can also be detected using only one miniVNA and their corresponding frequency splits can be used for motion characterization. Sensing multiple parameters requires the installment of multiple LC pairs and each pair can have different resonant frequency so that each occupies a different part of the entire frequency window. Different resonant frequencies can be achieved via soldering different capacitors or changing number of inductor loop. When their resonant frequencies don't overlap, multiple parameters can be sensed at the same time.

From the materials selection perspective, the LC sensors are not made of the most optimal material. Thin copper coils are flexible, but they are not stretchable. To achieve optimal wear comfort, the sensor should possess certain level of stretchability. One of the possible ways to improve the sensing coil's stretchability is to use polymer as a matrix material and fill the matrix with certain conductive materials. The polymer possesses the stretchability, and the conductive material ensures the device's high conductivity despite the presence of certain amount of strain.

In summary, these devices have many aspects that are worth improving in the future.

Reference

1. YIN, Y.; Zeng, Y.; Chen, X.; Fan, Y. The Internet of Things in Healthcare: An Overview. *J Ind Inf Integr* 2016, *1*, 3–13.
2. Habehh, H.; Gohel, S. Machine Learning in Healthcare. *Curr Genomics* **2021**, *22*, 291–300, doi:10.2174/1389202922666210705124359.
3. Callahan, A.; Shah, N.H. Machine Learning in Healthcare. In *Key Advances in Clinical Informatics: Transforming Health Care through Health Information Technology*; Elsevier, 2017; pp. 279–291 ISBN 9780128095232.
4. Heikenfeld, J.; Jajack, A.; Rogers, J.; Gutruf, P.; Tian, L.; Pan, T.; Li, R.; Khine, M.; Kim, J.; Wang, J.; et al. Wearable Sensors: Modalities, Challenges, and Prospects. *Lab Chip* 2018, *18*, 217–248.
5. Nguyen, T.; Khine, M. Advances in Materials for Soft Stretchable Conductors and Their Behavior under Mechanical Deformation. *Polymers (Basel)* 2020, *12*, 1–48.
6. Colin D. Mathers, A.D.L. and C.J.L.M. The Burden of Disease and Mortality by Condition: Data, Methods, and Results for 2001.
7. Thomas Gaziano, K.S.R.F.P.S.H. and V.C. Cardiovascular Disease.
8. Martsevich, S.Yu.; Semenova, Y. V.; Kutishenko, N.P.; Zagrebelnyy, A. V.; Ginzburg, M.L. Awareness of Cardiovascular Disease, Its Risk Factors, and Its Association with Attendance at Outpatient Clinics in Acute Coronary Syndrome Patients. *Integr Med Res* **2017**, *6*, 240–244, doi:10.1016/j.imr.2017.06.003.
9. Kuriachan, V.P.; Sumner, G.L.; Mitchell, L.B. Sudden Cardiac Death. *Curr Probl Cardiol* **2015**, *40*, 133–200, doi:10.1016/j.cpcardiol.2015.01.002.
10. Parsanathan, R.; Jain, S.K. Novel Invasive and Noninvasive Cardiac-Specific Biomarkers in Obesity and Cardiovascular Diseases. *Metab Syndr Relat Disord* 2020, *18*, 10–30.
11. Brzezinski, W.A. *6 Blood Pressure*;
12. Vidal-Petiot, E.; Greenlaw, N.; Ford, I.; Ferrari, R.; Fox, K.M.; Tardif, J.C.; Tendera, M.; Parkhomenko, A.; Bhatt, D.L.; Steg, P.G. Relationships between Components of Blood Pressure and Cardiovascular Events in Patients with Stable Coronary Artery Disease and Hypertension. *Hypertension* **2018**, *71*, 168–176, doi:10.1161/HYPERTENSIONAHA.117.10204.
13. Lawes, C.M.M.; Bennett, D.A.; Feigin, V.L.; Rodgers, A. Blood Pressure and Stroke: An Overview of Published Reviews. *Stroke* 2004, *35*, 776–785.
14. Eguchi, K.; Hoshide, S.; Schwartz, J.E.; Shimada, K.; Kario, K. Visit-to-Visit and Ambulatory Blood Pressure Variability as Predictors of Incident Cardiovascular Events in Patients with Hypertension. *Am J Hypertens* **2012**, *25*, 962–968, doi:10.1038/ajh.2012.75.

15. B, W.; G, M.; W, S.; E, A.R.; M, A.; M, B.; DL, C.; A, C.; G, de S.; A, D.; et al. 2018 ESC/ESH Guidelines for the Management of Arterial Hypertension. *Eur Heart J* **2018**, *39*, 3021–3104, doi:10.1093/EURHEARTJ/EHY339.

16. PK, W.; RM, C.; WS, A.; DE, C.; KJ, C.; C, D.H.; SM, D.; S, G.; KA, J.; DW, J.; et al. 2017 ACC/AHA/AAPA/ABC/ACPM/AGS/APhA/ASH/ASPC/NMA/PCNA Guideline for the Prevention, Detection, Evaluation, and Management of High Blood Pressure in Adults: Executive Summary: A Report of the American College of Cardiology/American Heart Association Task Force on Clinical Practice Guidelines. *Hypertension* **2018**, *71*, 1269–1324, doi:10.1161/HYP.0000000000000066.

17. Rwei, P.; Qian, C.; Abiri, A.; Zhou, Y.; Chou, E.F.; Tang, W.C.; Khine, M. Soft Iontronic Capacitive Sensor for Beat-to-Beat Blood Pressure Measurements. *Adv Mater Interfaces* **2022**, *9*, doi:10.1002/admi.202200294.

18. Bozkurt, B.; Ahmad, T.; Alexander, K.M.; Baker, W.L.; Bosak, K.; Breathett, K.; Fonarow, G.C.; Heidenreich, P.; Ho, J.E.; Hsich, E.; et al. Heart Failure Epidemiology and Outcomes Statistics: A Report of the Heart Failure Society of America. *J Card Fail* **2023**, *29*, 1412–1451, doi:10.1016/j.cardfail.2023.07.006.

19. Dunlay, S.M.; Weston, S.A.; Jacobsen, S.J.; Roger, V.L. Risk Factors for Heart Failure: A Population-Based Case-Control Study. *American Journal of Medicine* **2009**, *122*, 1023–1028, doi:10.1016/j.amjmed.2009.04.022.

20. Kapelios, C.J.; Lund, L.H. Preemptive Versus Urgent Heart Failure Hospitalization as a Surrogate for Mortality Risk in Heart Failure. *Circulation* **2024**, *149*, 1062–1064, doi:10.1161/CIRCULATIONAHA.123.068066.

21. De Couto, G.; Ouzounian, M.; Liu, P.P. Early Detection of Myocardial Dysfunction and Heart Failure. *Nat Rev Cardiol* 2010, *7*, 334–344.

22. White, J.A.; Patel, M.R. The Role of Cardiovascular MRI in Heart Failure and the Cardiomyopathies. *Magn Reson Imaging Clin N Am* 2007, *25*, 71–95.

23. Gehlbach, B.K.; Geppert, E. The Pulmonary Manifestations of Left Heart Failure*. *Chest* **2004**, *125*, 669–682, doi:10.1378/chest.125.2.669.

24. Kennedy, S.; Simon, B.; Alter, H.J.; Cheung, P. Ability of Physicians to Diagnose Congestive Heart Failure Based on Chest X-Ray. *Journal of Emergency Medicine* **2011**, *40*, 47–52, doi:10.1016/j.jemermed.2009.10.018.

25. Kelleher, K.; Kelly, J. The Electrocardiogram in Heart Failure. *Age Ageing* **2000**, *29*, 203–206, doi:10.1093/ageing/29.3.203.

26. Tang, W.H.W.; Tong, W. Measuring Impedance in Congestive Heart Failure: Current Options and Clinical Applications. *Am Heart J* 2009, *157*, 402–411.

27. Afari, M.E.; Syed, W.; Tsao, L. Implantable Devices for Heart Failure Monitoring and Therapy. *Heart Fail Rev* 2018, *23*, 935–944.

28. Volterrani, M.; Spoletini, I.; Angermann, C.; Rosano, G.; Coats, A.J. Implantable Devices for Heart Failure Monitoring: The CardioMEMS^{TM} System. *European Heart Journal, Supplement* **2019**, *21*, M50–M53, doi:10.1093/eurheartj/suz265.

29. Ye, F.; Hajiaghajani, A.; Zargari, A.; Escobar, A.; Qin, H.; Li, L.; Qian, C.; Dia, K.K.H.; Hasan, M.A.; Dautta, M.; et al. Passive Wireless Body Joint-Monitoring Networks with Textile-Integrated, Strongly Coupled Magnetic Resonators. *Adv Electron Mater* **2024**, doi:10.1002/aelm.202400450.

30. Kim, J.; Chou, E.; Le, J.; Wong, S.; Chu, M.; Khine, M. Soft Wearable Pressure Sensors for Beat-to-Beat Blood Pressure Monitoring. *Adv Healthc Mater* **2019**, *8*, 1900109, doi:10.1002/adhm.201900109.

31. Jeong, H.; Ha, T.; Kuang, I.; Shen, L.; Dai, Z.; Sun, N.; Lu, N. *NFC-Enabled, Tattoo-Like Stretchable Biosensor Manufactured by •Cut-And-Paste• Method*; 2017; ISBN 9781509028092.

32. Zamarayeva, A.M.; Ostfeld, A.E.; Wang, M.; Duey, J.K.; Deckman, I.; Lechêne, B.P.; Davies, G.; Steingart, D.A.; Arias, A.C. *Flexible and Stretchable Power Sources for Wearable Electronics*; 2017;

33. Keum, K.; Kim, J.W.; Hong, S.Y.; Son, J.G.; Lee, S.S.; Ha, J.S. Flexible/Stretchable Supercapacitors with Novel Functionality for Wearable Electronics. *Advanced Materials* 2020, *32*.

34. Chu, M.; Nguyen, T.; Pandey, V.; Zhou, Y.; Pham, H.N.; Bar-Yoseph, R.; Radom-Aizik, S.; Jain, R.; Cooper, D.M.; Khine, M. Respiration Rate and Volume Measurements Using Wearable Strain Sensors. *NPJ Digit Med* **2019**, *2*, doi:10.1038/s41746-019-0083-3.

35. Niu, S.; Matsuhisa, N.; Beker, L.; Li, J.; Wang, S.; Wang, J.; Jiang, Y.; Yan, X.; Yun, Y.; Burnett, W.; et al. A Wireless Body Area Sensor Network Based on Stretchable Passive Tags. *Nat Electron* **2019**, *2*, 361–368, doi:10.1038/s41928-019-0286-2.

36. Guo, R.; Wang, X.; Yu, W.; Tang, J.; Liu, J. A Highly Conductive and Stretchable Wearable Liquid Metal Electronic Skin for Long-Term Conformable Health Monitoring. *Sci China Technol Sci* **2018**, *61*, 1031–1037, doi:10.1007/s11431-018-9253-9.

37. Kim, Y.S.; Mahmood, M.; Lee, Y.; Kim, N.K.; Kwon, S.; Herbert, R.; Kim, D.; Cho, H.C.; Yeo, W.H. All-in-One, Wireless, Stretchable Hybrid Electronics for Smart, Connected, and Ambulatory Physiological Monitoring. *Advanced Science* **2019**, *6*, doi:10.1002/advs.201900939.

38. Votzke, C.; Daalkhaijav, U.; Menguc, Y.; Johnston, M.L. 3D-Printed Liquid Metal Interconnects for Stretchable Electronics. *IEEE Sens J* **2019**, *19*, 3832–3840, doi:10.1109/JSEN.2019.2894405.

39. Huang, Z.; Hao, Y.; Li, Y.; Hu, H.; Wang, C.; Nomoto, A.; Pan, T.; Gu, Y.; Chen, Y.; Zhang, T.; et al. Three-Dimensional Integrated Stretchable Electronics. *Nat Electron* **2018**, *1*, 473–480, doi:10.1038/s41928-018-0116-y.

40. Li, Y.; Liu, W.; Deng, Y.; Hong, W.; Yu, H. Miura-Ori Enabled Stretchable Circuit Boards. *npj Flexible Electronics* **2021**, *5*, doi:10.1038/s41528-021-00099-8.

41. Li, Y.; Yu, H. A Planar Developable Double Corrugation Surface Enabled Stretchable Heart Rate Sensing System. *IEEE Sens J* **2021**, *21*, 16275–16281, doi:10.1109/JSEN.2021.3076108.

42. Song, E.; Xie, Z.; Bai, W.; Luan, H.; Ji, B.; Ning, X.; Xia, Y.; Baek, J.M.; Lee, Y.; Avila, R.; et al. Miniaturized Electromechanical Devices for the Characterization of the Biomechanics of Deep Tissue. *Nat Biomed Eng* **2021**, *5*, 759–771, doi:10.1038/s41551-021-00723-y.

43. Xu, S.; Zhang, Y.; Jia, L.; Mathewson, K.E.; Jang, K.-I.; Kim, J.; Fu, H.; Huang, X.; Chava, P.; Wang, R.; et al. *Soft Microfluidic Assemblies of Sensors, Circuits, and Radios for the Skin*;

44. Lin, S.; Zhang, D.; Wang, Y.; Yu, Z.; Li, Q.; Wang, F.; Li, Y.; Guo, Y.; Miao, J.; Cui, D.; et al. A Cost-Effective and Solderability Stretchable Circuit Boards for Wearable Devices. *Sens Actuators A Phys* **2021**, *331*, 112924, doi:10.1016/j.sna.2021.112924.

45. Rajesh; Ahuja, T.; Kumar, D. Recent Progress in the Development of Nano-Structured Conducting Polymers/Nanocomposites for Sensor Applications. *Sens Actuators B Chem* 2009, *136*, 275–286.

46. Stassi, S.; Cauda, V.; Canavese, G.; Pirri, C.F. Flexible Tactile Sensing Based on Piezoresistive Composites: A Review. *Sensors (Switzerland)* 2014, *14*, 5296–5332.

47. Niu, X.; Peng, S.; Liu, L.; Wen, W.; Sheng, P. Characterizing and Patterning of PDMS-Based Conducting Composites. *Advanced Materials* **2007**, *19*, 2682–2686, doi:10.1002/adma.200602515.

48. Kong, M.; You, I.; Lee, G.; Park, G.; Kim, J.; Park, D.; Jeong, U. Transparent Omni-Directional Stretchable Circuit Lines Made by a Junction-Free Grid of Expandable Au Lines. *Advanced Materials* **2021**, *33*, doi:10.1002/adma.202100299.

49. Zhou, Y.; Werner, E.M.; Lee, E.; Chu, M.; Nguyen, T.; Costa, K.D.; Hui, E.E.; Khine, M. High-Resolution Integrated Piezoresistive Sensors for Microfluidic Monitoring. *Lab Chip* **2021**, *21*, 83–92, doi:10.1039/D0LC01046D.

50. Kim, J.; Park, S.-J.; Nguyen, T.; Chu, M.; Pegan, J.D.; Khine, M. Highly Stretchable Wrinkled Gold Thin Film Wires. *Appl Phys Lett* **2016**, *108*, 061901, doi:10.1063/1.4941439.

51. Raton, B.; New, L.; Washington, Y.; Madou, M.J. *CRC PR E S S The Science of Miniaturization Second Edition*;

52. Lakhal, K.; Ehrmann, S.; Boulain, T. Noninvasive BP Monitoring in the Critically Ill: Time to Abandon the Arterial Catheter? *Chest* 2018, *153*, 1023–1039.

53. Meidert, A.S.; Saugel, B. Techniques for Non-Invasive Monitoring of Arterial Blood Pressure. *Front Med (Lausanne)* **2017**, *4*, 1–6, doi:10.3389/fmed.2017.00231.

54. Chung, E.; Chen, G.; Alexander, B.; Cannesson, M. Non-Invasive Continuous Blood Pressure Monitoring: A Review of Current Applications. *Front Med China* **2013**, *7*, 91–101, doi:10.1007/s11684-013-0239-5.

55. Fortin, J.; Rogge, D.E.; Fellner, C.; Flotzinger, D.; Grond, J.; Lerche, K.; Saugel, B. A Novel Art of Continuous Noninvasive Blood Pressure Measurement. *Nat Commun* **2021**, *12*, doi:10.1038/s41467-021-21271-8.

56. Nelson, M.R.; Stepanek, J.; Cevette, M.; Covalciuc, M.; Hurst, R.T.; Tajik, A.J. Noninvasive Measurement of Central Vascular Pressures with Arterial Tonometry: Clinical Revival of the Pulse Pressure Waveform? *Mayo Clin Proc* **2010**, *85*, 460–472, doi:10.4065/mcp.2009.0336.

57. Choong, C.L.; Shim, M.B.; Lee, B.S.; Jeon, S.; Ko, D.S.; Kang, T.H.; Bae, J.; Lee, S.H.; Byun, K.E.; Im, J.; et al. Highly Stretchable Resistive Pressure Sensors Using a Conductive Elastomeric Composite on a Micropyramid Array. *Advanced Materials* **2014**, *26*, 3451–3458, doi:10.1002/adma.201305182.

58. Pang, C.; Lee, G.Y.; Kim, T. Il; Kim, S.M.; Kim, H.N.; Ahn, S.H.; Suh, K.Y. A Flexible and Highly Sensitive Strain-Gauge Sensor Using Reversible Interlocking of Nanofibres. *Nat Mater* **2012**, *11*, 795–801, doi:10.1038/nmat3380.

59. Wang, X.; Gu, Y.; Xiong, Z.; Cui, Z.; Zhang, T. Silk-Molded Flexible, Ultrasensitive, and Highly Stable Electronic Skin for Monitoring Human Physiological Signals. *Advanced Materials* **2014**, *26*, 1336–1342, doi:10.1002/adma.201304248.

60. Yue, Y.; Liu, N.; Ma, Y.; Wang, S.; Liu, W.; Luo, C.; Zhang, H.; Cheng, F.; Rao, J.; Hu, X.; et al. Highly Self-Healable 3D Microsupercapacitor with MXene-Graphene Composite Aerogel. *ACS Nano* **2018**, *12*, 4224–4232, doi:10.1021/acsnano.7b07528.

61. Ciocchetti, M.; Massaroni, C.; Saccomandi, P.; Caponero, M.A.; Polimadei, A.; Formica, D.; Schena, E. Smart Textile Based on Fiber Bragg Grating Sensors for Respiratory Monitoring: Design and Preliminary Trials. *Biosensors (Basel)* **2015**, *5*, 602–615, doi:10.3390/bios5030602.

62. Fajkus, M.; Nedoma, J.; Martinek, R.; Vasinek, V.; Nazeran, H.; Siska, P. A Non-Invasive Multichannel Hybrid Fiber-Optic Sensor System for Vital Sign Monitoring. *Sensors (Switzerland)* **2017**, *17*, 1–17, doi:10.3390/s17010111.

63. Dziuda, Ł.; Skibniewski, F.W. A New Approach to Ballistocardiographic Measurements Using Fibre Bragg Grating-Based Sensors. *Biocybern Biomed Eng* **2014**, *34*, 101–116, doi:10.1016/j.bbe.2014.02.001.

64. Chu, Y.; Zhong, J.; Liu, H.; Ma, Y.; Liu, N.; Song, Y.; Liang, J.; Shao, Z.; Sun, Y.; Dong, Y.; et al. Human Pulse Diagnosis for Medical Assessments Using a Wearable Piezoelectret Sensing System. *Adv Funct Mater* **2018**, *28*, doi:10.1002/adfm.201803413.

65. Park, J.; Kim, M.; Lee, Y.; Lee, H.S.; Ko, H. Nanomaterials: Fingertip Skin-Inspired Microstructured Ferroelectric Skins Discriminate Static/Dynamic Pressure and Temperature Stimuli. *Sci Adv* **2015**, *1*, doi:10.1126/sciadv.1500661.

66. Su, Y.; Chen, C.; Pan, H.; Yang, Y.; Chen, G.; Zhao, X.; Li, W.; Gong, Q.; Xie, G.; Zhou, Y.; et al. Muscle Fibers Inspired High-Performance Piezoelectric Textiles for Wearable Physiological Monitoring. *Adv Funct Mater* **2021**, *31*, doi:10.1002/adfm.202010962.

67. Park, D.Y.; Joe, D.J.; Kim, D.H.; Park, H.; Han, J.H.; Jeong, C.K.; Park, H.; Park, J.G.; Joung, B.; Lee, K.J. Self-Powered Real-Time Arterial Pulse Monitoring Using Ultrathin Epidermal Piezoelectric Sensors. *Advanced Materials* **2017**, *29*, 1–9, doi:10.1002/adma.201702308.

68. Dagdeviren, C.; Su, Y.; Joe, P.; Yona, R.; Liu, Y.; Kim, Y.S.; Huang, Y.; Damadoran, A.R.; Xia, J.; Martin, L.W.; et al. Conformable Amplified Lead Zirconate Titanate Sensors with Enhanced Piezoelectric Response for Cutaneous Pressure Monitoring. *Nat Commun* **2014**, *5*, doi:10.1038/ncomms5496.

69. Ha, M.; Lim, S.; Cho, S.; Lee, Y.; Na, S.; Baig, C.; Ko, H. Skin-Inspired Hierarchical Polymer Architectures with Gradient Stiffness for Spacer-Free, Ultrathin, and Highly Sensitive Triboelectric Sensors. *ACS Nano* **2018**, *12*, 3964–3974, doi:10.1021/acsnano.8b01557.

70. Ouyang, H.; Tian, J.; Sun, G.; Zou, Y.; Liu, Z.; Li, H.; Zhao, L.; Shi, B.; Fan, Y.; Fan, Y.; et al. Self-Powered Pulse Sensor for Antidiastole of Cardiovascular Disease. *Advanced Materials* **2017**, *29*, 1–10, doi:10.1002/adma.201703456.

71. Wang, X.; Yang, J.; Meng, K.; He, Q.; Zhang, G.; Zhou, Z.; Tan, X.; Feng, Z.; Sun, C.; Yang, J.; et al. Enabling the Unconstrained Epidermal Pulse Wave Monitoring via Finger-Touching. *Adv Funct Mater* **2021**, *31*, doi:10.1002/adfm.202102378.

72. Yang, J.; Chen, J.; Su, Y.; Jing, Q.; Li, Z.; Yi, F.; Wen, X.; Wang, Z.; Wang, Z.L. Eardrum-Inspired Active Sensors for Self-Powered Cardiovascular System Characterization and Throat-Attached Anti-Interference Voice Recognition. *Advanced Materials* **2015**, *27*, 1316–1326, doi:10.1002/adma.201404794.

73. Zhao, X.; Zhou, Y.; Xu, J.; Chen, G.; Fang, Y.; Tat, T.; Xiao, X.; Song, Y.; Li, S.; Chen, J. Soft Fibers with Magnetoelasticity for Wearable Electronics. *Nat Commun* **2021**, *12*, doi:10.1038/s41467-021-27066-1.

74. Zhou, Y.; Zhao, X.; Xu, J.; Fang, Y.; Chen, G.; Song, Y.; Li, S.; Chen, J. Giant Magnetoelastic Effect in Soft Systems for Bioelectronics. *Nat Mater* **2021**, *20*, 1670–1676, doi:10.1038/s41563-021-01093-1.

75. Meng, K.; Xiao, X.; Wei, W.; Chen, G.; Nashalian, A.; Shen, S.; Xiao, X.; Chen, J. Wearable Pressure Sensors for Pulse Wave Monitoring. *Advanced Materials* **2022**, 2109357, doi:10.1002/adma.202109357.

76. Mannsfeld, S.C.B.; Tee, B.C.-K.; Stoltenberg, R.M.; Chen, C.V.H.-H.; Barman, S.; Muir, B.V.O.; Sokolov, A.N.; Reese, C.; Bao, Z. Highly Sensitive Flexible Pressure Sensors with Microstructured Rubber Dielectric Layers. *Nature Materials 2010 9:10* **2010**, *9*, 859–864, doi:10.1038/nmat2834.

77. Yang, J.; Luo, S.; Zhou, X.; Li, J.; Fu, J.; Yang, W.; Wei, D. Flexible, Tunable, and Ultrasensitive Capacitive Pressure Sensor with Microconformal Graphene Electrodes. *ACS Appl Mater Interfaces* **2019**, *11*, 14997–15006, doi:10.1021/ACSAMI.9B02049.

78. Xu, F.; Zhu, Y. Highly Conductive and Stretchable Silver Nanowire Conductors. *Advanced Materials* **2012**, *24*, 5117–5122, doi:10.1002/ADMA.201201886.

79. Zeng, X.; Wang, Z.; Zhang, H.; Yang, W.; Xiang, L.; Zhao, Z.; Peng, L.M.; Hu, Y. Tunable, Ultrasensitive, and Flexible Pressure Sensors Based on Wrinkled Microstructures for Electronic Skins. *ACS Appl Mater Interfaces* **2019**, *11*, 21218–21226, doi:10.1021/acsami.9b02518.

80. Boutry, C.M.; Negre, M.; Jorda, M.; Vardoulis, O.; Chortos, A.; Khatib, O.; Bao, Z. A Hierarchically Patterned, Bioinspired e-Skin Able to Detect the Direction of Applied Pressure for Robotics. *Sci Robot* **2018**, *3*, doi:10.1126/SCIROBOTICS.AAU6914.

81. Luo, Y.; Shao, J.; Chen, S.; Chen, X.; Tian, H.; Li, X.; Wang, L.; Wang, D.; Lu, B. Flexible Capacitive Pressure Sensor Enhanced by Tilted Micropillar Arrays. *ACS Appl Mater Interfaces* **2019**, *11*, 17796–17803, doi:10.1021/ACSAMI.9B03718.

82. Yang, J.C.; Kim, J.-O.; Oh, J.; Kwon, S.Y.; Sim, J.Y.; Kim, D.W.; Choi, H.B.; Park, S. Microstructured Porous Pyramid-Based Ultrahigh Sensitive Pressure Sensor Insensitive to Strain and Temperature. *ACS Appl Mater Interfaces* **2019**, *11*, 19472–19480, doi:10.1021/ACSAMI.9B03261.

83. Baek, S.; Jang, H.; Kim, S.Y.; Jeong, H.; Han, S.; Jang, Y.; Kim, D.H.; Lee, H.S. Flexible Piezocapacitive Sensors Based on Wrinkled Microstructures: Toward Low-Cost Fabrication of Pressure Sensors over Large Areas. *RSC Adv* **2017**, *7*, 39420–39426, doi:10.1039/C7RA06997A.

84. Liu, F.; Han, F.; Ling, L.; Li, J.; Zhao, S.; Zhao, T.; Liang, X.; Zhu, D.; Zhang, G.; Sun, R.; et al. An Omni-Healable and Highly Sensitive Capacitive Pressure Sensor with Microarray Structure. *Chemistry – A European Journal* **2018**, *24*, 16823–16832, doi:10.1002/CHEM.201803369.

85. Pruvost, M.; Smit, W.J.; Monteux, C.; Poulin, P.; Colin, A. Polymeric Foams for Flexible and Highly Sensitive Low-Pressure Capacitive Sensors. *npj Flexible Electronics 2019 3:1* **2019**, *3*, 1–6, doi:10.1038/s41528-019-0052-6.

86. Qi, D.; Zhang, K.; Tian, G.; Jiang, B.; Huang, Y. Stretchable Electronics Based on PDMS Substrates. *Advanced Materials* **2021**, *33*, 1–25, doi:10.1002/adma.202003155.

87. Pegan, J.D.; Zhang, J.; Chu, M.; Nguyen, T.; Park, S.-J.; Paul, A.; Kim, J.; Bachman, M.; Khine, M. Skin-Mountable Stretch Sensor for Wearable Health Monitoring. *Nanoscale* **2016**, *8*, 17295–17303, doi:10.1039/C6NR04467K.

88. Yang, X.; Wang, Y.; Qing, X. A Flexible Capacitive Pressure Sensor Based on Ionic Liquid. *Sensors (Switzerland)* **2018**, *18*, doi:10.3390/s18072395.

89. Cho, S.H.; Lee, S.W.; Yu, S.; Kim, H.; Chang, S.; Kang, D.; Hwang, I.; Kang, H.S.; Jeong, B.; Kim, E.H.; et al. Micropatterned Pyramidal Ionic Gels for Sensing Broad-Range Pressures with High Sensitivity. *ACS Appl Mater Interfaces* **2017**, *9*, 10128–10135, doi:10.1021/acsami.7b00398.

90. Chhetry, A.; Kim, J.; Yoon, H.; Park, J.Y. Ultrasensitive Interfacial Capacitive Pressure Sensor Based on a Randomly Distributed Microstructured Iontronic Film for Wearable Applications. *ACS Appl Mater Interfaces* **2019**, *11*, 3438–3449, doi:10.1021/acsami.8b17765.

91. Xiong, Y.; Shen, Y.; Tian, L.; Hu, Y.; Zhu, P.; Sun, R.; Wong, C.P. A Flexible, Ultra-Highly Sensitive and Stable Capacitive Pressure Sensor with Convex Microarrays for Motion and Health Monitoring. *Nano Energy* **2020**, *70*, 104436, doi:10.1016/j.nanoen.2019.104436.

92. Li, W.; Jin, X.; Zheng, Y.; Chang, X.; Wang, W.; Lin, T.; Zheng, F.; Onyilagha, O.; Zhu, Z. A Porous and Air Gap Elastomeric Dielectric Layer for Wearable Capacitive Pressure Sensor with High Sensitivity and a Wide Detection Range. *J Mater Chem C Mater* **2020**, *8*, 11468–11476, doi:10.1039/d0tc00443j.

93. Hwang, J.; Kim, Y.; Yang, H.; Oh, J.H. Fabrication of Hierarchically Porous Structured PDMS Composites and Their Application as a Flexible Capacitive Pressure Sensor. *Compos B Eng* **2021**, *211*, 108607, doi:10.1016/j.compositesb.2021.108607.

94. Kumar, S.; Bijender; Yadav, S.; Kumar, A. Flexible Microhyperboloids Facets Giant Sensitive Ultra-Low Pressure Sensor. *Sens Actuators A Phys* **2021**, *328*, 112767, doi:10.1016/j.sna.2021.112767.

95. Zhang, Z.; Gui, X.; Hu, Q.; Yang, L.; Yang, R.; Huang, B.; Yang, B.R.; Tang, Z. Highly Sensitive Capacitive Pressure Sensor Based on a Micropyramid Array for Health and Motion Monitoring. *Adv Electron Mater* **2021**, *7*, 1–8, doi:10.1002/aelm.202100174.

96. Liu, Q.; Liu, Z.; Li, C.; Xie, K.; Zhu, P.; Shao, B.; Zhang, J.; Yang, J.; Zhang, J.; Wang, Q.; et al. Highly Transparent and Flexible Iontronic Pressure Sensors Based on an Opaque to Transparent Transition. *Advanced Science* **2020**, *7*, doi:10.1002/advs.202000348.

97. Joo, Y.; Byun, J.; Seong, N.; Ha, J.; Kim, H.; Kim, S.; Kim, T.; Im, H.; Kim, D.; Hong, Y. Silver Nanowire-Embedded PDMS with a Multiscale Structure for a Highly Sensitive and Robust Flexible Pressure Sensor. *Nanoscale* **2015**, *7*, 6208–6215, doi:10.1039/c5nr00313j.

98. Li, T.; Luo, H.; Qin, L.; Wang, X.; Xiong, Z.; Ding, H.; Gu, Y.; Liu, Z.; Zhang, T. Flexible Capacitive Tactile Sensor Based on Micropatterned Dielectric Layer. *Small* **2016**, *12*, 5042–5048, doi:10.1002/smll.201600760.

99. Pang, C.; Koo, J.H.; Nguyen, A.; Caves, J.M.; Kim, M.G.; Chortos, A.; Kim, K.; Wang, P.J.; Tok, J.B.H.; Bao, Z. Highly Skin-Conformal Microhairy Sensor for Pulse Signal Amplification. *Advanced Materials* **2015**, *27*, 634–640, doi:10.1002/adma.201403807.

100. Lin, Q.; Huang, J.; Yang, J.; Huang, Y.; Zhang, Y.; Wang, Y.; Zhang, J.; Wang, Y.; Yuan, L.; Cai, M.; et al. Highly Sensitive Flexible Iontronic Pressure Sensor for Fingertip Pulse Monitoring. *Adv Healthc Mater* **2020**, *9*, 2001023, doi:10.1002/ADHM.202001023.

101. Takazawa, K.; Kobayashi, H.; Shindo, N. Relationship between Radial and Central Arterial Pulse Wave and Evaluation of Central Aortic. **2007**, *30*, 219–228.

102. Banhatti, R.D.; Funke, K. Dielectric Function and Localized Diffusion in Ion Conducting Glasses. *Solid State Ion* **2004**, *175*, 661–663, doi:10.1016/j.ssi.2004.09.063.

103. Arya, A.; Sadiq, Mohd.; Sharma, A.L. Salt Concentration and Temperature Dependent Dielectric Properties of Blend Solid Polymer Electrolyte Complexed with NaPF6. *Mater Today Proc* **2019**, *12*, 554–564, doi:10.1016/j.matpr.2019.03.098.

104. Fortin, J.; Lerche, K.; Flotzinger, D.; O'Brien, T. Is the Standard Supplied by the Association for the Advancement of Medical Instrumentation the Measure of All Things for Noninvasive Continuous Hemodynamic Devices? *Anesthesiology* **2015**, *122*, 208–209, doi:10.1097/ALN.0000000000000485.

105. Xu, S.; Rwei, A.Y.; Vwalika, B.; Chisembele, M.P.; Stringer, J.S.A.; Ginsburg, A.S.; Rogers, J.A. Wireless Skin Sensors for Physiological Monitoring of Infants in Low-Income and Middle-Income Countries. *Lancet Digit Health* 2021, *3*, e266–e273.

106. Li, J.; Jia, H.; Zhou, J.; Huang, X.; Xu, L.; Jia, S.; Gao, Z.; Yao, K.; Li, D.; Zhang, B.; et al. Thin, Soft, Wearable System for Continuous Wireless Monitoring of Artery Blood Pressure. *Nat Commun* **2023**, *14*, doi:10.1038/s41467-023-40763-3.

107. Rothman, A.M.K.; Zafar, H.; Sandy, R.; Wright, C.; Mitra, S.; Ebah, L.; Ilyas, D.; Hanumapura, P.; Sebastien, S.; Khalifa, A.; et al. A Subcutaneous Multiparameter Sensor With Integrated Interstitial Fluid Pressure Measurement for Remote Heart Failure Monitoring. *JACC Basic Transl Sci* **2023**, *8*, 386–388, doi:10.1016/j.jacbts.2023.03.004.

108. Orban, M.; Bruce, C.J.; Pressman, G.S.; Leinveber, P.; Romero-Corral, A.; Korinek, J.; Konecny, T.; Villarraga, H.R.; Kara, T.; Caples, S.M.; et al. Dynamic Changes of Left Ventricular Performance and Left Atrial Volume Induced by the Mueller Maneuver in Healthy Young Adults and Implications for Obstructive Sleep Apnea, Atrial Fibrillation, and Heart Failure. *American Journal of Cardiology* **2008**, *102*, 1557–1561, doi:10.1016/j.amjcard.2008.07.050.

109. Kemp, C.D.; Conte, J. V. The Pathophysiology of Heart Failure. *Cardiovascular Pathology* **2012**, *21*, 365–371, doi:10.1016/j.carpath.2011.11.007.

110. Dharmarajan, K.; Hsieh, A.F.; Lin, Z.; Bueno, H.; Ross, J.S.; Horwitz, L.I.; Barreto-Filho, J.A.; Kim, N.; Bernheim, S.M.; Suter, L.G.; et al. Diagnoses and Timing of 30-Day Readmissions after Hospitalization for Heart Failure, Acute Myocardial Infarction, or Pneumonia. *JAMA* **2013**, *309*, 355–363, doi:10.1001/jama.2012.216476.

111. Rubini, A.; Vilaplana-Prieto, C.; Vázquez-Jarén, E.; Hernández-González, M.; Félix-Redondo, F.J.; Fernández-Bergés, D. Analysis and Prediction of Readmissions for Heart Failure in the First Year after Discharge with INCA Score. *Sci Rep* **2023**, *13*, doi:10.1038/s41598-023-49390-w.

112. Bose Brill, S.; Riley, S.R.; Prater, L.; Schnell, P.M.; Schuster, A.L.R.; Smith, S.A.; Foreman, B.; Xu, W.Y.; Gustin, J.; Li, Y.; et al. Advance Care Planning (ACP) in Medicare Beneficiaries with Heart Failure. *J Gen Intern Med* **2024**, doi:10.1007/s11606-024-08604-1.

113. Desai, A.S. The Three-Phase Terrain of Heart Failure Readmissions. *Circ Heart Fail* **2012**, *5*, 398–400, doi:10.1161/CIRCHEARTFAILURE.112.968735.

114. Butler, B.; Kalogeropoulos, A.; Georgiopoulou, V.; Belue, R.; Rodondi, N.; Garcia, M.; Bauer, D.C.; Satterfield, S.; Smith, A.L.; Vaccarino, V.; et al. Incident Heart Failure Prediction in the Elderly: The Health ABC Heart Failure Score. *Circ Heart Fail* **2008**, *1*, 125–133, doi:10.1161/CIRCHEARTFAILURE.108.768457.

115. Reinhardt, S.W.; Clark, K.A.A.; Xin, X.; Parzynski, C.S.; Riello, R.J.; Sarocco, P.; Ahmad, T.; Desai, N.R. Thirty-Day and 90-Day Episode of Care Spending Following Heart Failure Hospitalization among Medicare Beneficiaries. *Circ Cardiovasc Qual Outcomes* **2022**, *15*, E008069, doi:10.1161/CIRCOUTCOMES.121.008069.

116. Okada, A.; Tsuchihashi-Makaya, M.; Kang, J.; Aoki, Y.; Fukawa, M.; Matsuoka, S. Symptom Perception, Evaluation, Response to Symptom, and Delayed Care Seeking in Patients with Acute Heart Failure: An Observational Study. *Journal of Cardiovascular Nursing* **2019**, *34*, 36–43, doi:10.1097/JCN.0000000000000526.

117. Lin, C.Y.; Dracup, K.; Pelter, M.M.; Biddle, M.J.; Moser, D.K. Association of Psychological Distress with Reasons for Delay in Seeking Medical Care in Rural Patients with Worsening Heart Failure Symptoms. *Journal of Rural Health* **2022**, *38*, 713–720, doi:10.1111/jrh.12573.

118. Lin, C.Y.; Hammash, M.; Miller, J.L.; Schrader, M.; Mudd-Martin, G.; Biddle, M.J.; Moser, D.K. Delay in Seeking Medical Care for Worsening Heart Failure Symptoms: Predictors and Association with Cardiac Events. *European Journal of Cardiovascular Nursing* **2021**, *20*, 454–463, doi:10.1093/eurjcn/zvaa032.

119. Wexler, R.; Elton, T.; Pleister, A.; Feldman, D. Cardiomyopathy: An Overview. *Am Fam Physician* **2009**, *79*, 778–784.

120. Ponikowski, P.; Spoletini, I.; Coats, A.J.S.; Piepoli, M.F.; Rosano, G.M.C. Heart Rate and Blood Pressure Monitoring in Heart Failure. *European Heart Journal, Supplement* **2019**, *21*, M13–M16, doi:10.1093/eurheartj/suz217.

121. Oh, G.C.; Cho, H.J. Blood Pressure and Heart Failure. *Clin Hypertens* 2020, *26*.

122. Tegtmeyer, K.; Brady, G.; Lai, S.; Hodo, R.; Braner, D. Placement of an Arterial Line. *N Engl J Med* **2006**, *354*, doi:10.1056/NEJMvcm044149.

123. Adamson, P.B.; Magalski, A.; Braunschweig, F.; Böhm, M.; Reynolds, D.; Steinhaus, D.; Luby, A.; Linde, C.; Ryden, L.; Cremers, B.; et al. Ongoing Right Ventricular Hemodynamics in Heart Failure: Clinical Value of Measurements Derived from an Implantable Monitoring System. *J Am Coll Cardiol* **2003**, *41*, 565–571, doi:10.1016/S0735-1097(02)02896-6.

124. Ritzema, J.; Melton, I.C.; Richards, A.M.; Crozier, I.G.; Frampton, C.; Doughty, R.N.; Whiting, J.; Kar, S.; Eigler, N.; Krum, H.; et al. Direct Left Atrial Pressure Monitoring in Ambulatory Heart Failure Patients: Initial Experience with a New Permanent Implantable Device. *Circulation* **2007**, *116*, 2952–2959, doi:10.1161/CIRCULATIONAHA.107.702191.

125. Raina, A.; Benza, R.L. Ambulatory Hemodynamic Monitoring in the Management of Pulmonary Arterial Hypertension. *Adv Pulm Hypertens* **2014**, *13*, 81–85, doi:10.21693/1933-088x-13.2.81.

126. Reghunathan, A.; Chick, J.F.B.; Gemmete, J.J.; Hage, A.; Mahn, J.; Khaja, M.S.; Srinivasa, R.N. Endovascular Retrieval of a CardioMEMS Heart Failure System. *Radiol Case Rep* **2018**, *13*, 386–388, doi:10.1016/j.radcr.2018.01.013.

127. Cho, S.; Atwood, J.E. Peripheral Edema. *American Journal of Medicine* **2002**, *113*, 580–586, doi:10.1016/S0002-9343(02)01322-0.

128. Burch, George, E.; DePasquale, N.P. Congestive Heart Failure-Acute Pulmonary Edema. *JAMA* **1969**, *208*, 1895–1897, doi:10.1001/jama.208.10.1895.

129. Kumarasinghe, G.; Carroll, G. A Guide to Peripheral Oedema. *Med Today* **2015**, *16*, 26–34.

130. Guyton, A.C.; Coleman, T.G. REGULATION OF INTERSTITIAL FLUID VOLUME AND PRESSURE. *Ann N Y Acad Sci* **1968**, *150*, 537–547, doi:10.1111/j.1749-6632.1968.tb14705.x.

131. Guyton, A.C.; Granger, H.J.; Taylor, A.E. Interstitial Fluid Pressure. *Physiol Rev* **1971**, *51*, 527–563, doi:10.1152/physrev.1971.51.3.527.

132. Guyton, A.C. A Concept of Negative Interstitial Pressure Based on Pressures in Implanted Perforated Capsules. **1963**, *12*, 399–414, doi:10.1161/01.res.12.4.399.

133. Fallahzadeh, R.; Pedram, M.; Ghasemzadeh, H. SmartSock: A Wearable Platform for Context-Aware Assessment of Ankle Edema. In Proceedings of the Proceedings of the Annual International Conference of the IEEE Engineering in Medicine and Biology Society, EMBS; Institute of Electrical and Electronics Engineers Inc., October 13 2016; Vol. 2016-October, pp. 6302–6306.

134. Huang, X.; Liu, Y.; Cheng, H.; Shin, W.J.; Fan, J.A.; Liu, Z.; Lu, C.J.; Kong, G.W.; Chen, K.; Patnaik, D.; et al. Materials and Designs for Wireless Epidermal Sensors of Hydration and Strain. *Adv Funct Mater* **2014**, *24*, 3846–3854, doi:10.1002/adfm.201303886.

135. Yu, F.; Bilberg, A.; Xiao, L.; Yderstraede, K.B. Foot Edema Simulation and Monitoring Using Dielectric Electro-Active Polymer Sensors. *Sens Actuators A Phys* **2015**, *225*, 33–40, doi:10.1016/j.sna.2015.02.005.

136. Kim, S.; Iravantchi, Y.; Gajos, K.Z. *SwellFit: Developing A Wearable Sensor for Monitoring Peripheral Edema*;

137. Gehin, C.; Grenier, E.; Chaigneau, C.; Reinaudo, J.; Claude, A.; Massot, B.; Montalibet, A.; McAdams, E.T. Ambulatory Sensor for the Monitoring of the Edema Circumference in Lower Limbs. *Sens Actuators A Phys* **2018**, *272*, 83–91, doi:10.1016/j.sna.2018.01.036.

138. Fallahzadeh, R.; Ma, Y.; Ghasemzadeh, H. Context-Aware System Design for Remote Health Monitoring: An Application to Continuous Edema Assessment. *IEEE Trans Mob Comput* **2017**, *16*, 2159–2173, doi:10.1109/TMC.2016.2616403.

139. Yamada, E.F.; Balbin Villaverde, A.G.J.; Munin, E.; Zangaro, R.A.; Pacheco, M.T.T. Effect of Low-Power Laser Therapy on Edema Dynamics: Sensing by Using the Electrical Capacitance Method. *Laser Interaction with Tissue and Cells XV* **2004**, *5319*, 355–362, doi:10.1117/12.528105.

140. Ozerdem, U.; Hargens, A.R. A Simple Method for Measuring Interstitial Fluid Pressure in Cancer Tissues. *Microvasc Res* **2005**, *70*, 116–120, doi:10.1016/j.mvr.2005.07.003.

141. Scholander, P.F.; Hargens, A.R.; Miller, S.L. Negative Pressure in the Interstitial Fluid of Animals. *New Series* **1968**, *161*, 321–328, doi:10.1126/science.161.3839.321.

142. Ozerdem, U. Measuring Interstitial Fluid Pressure with Fiberoptic Pressure Transducers. *Microvasc Res* **2009**, *77*, 226–229, doi:10.1016/j.mvr.2008.08.002.

143. Fadnes, H.O.; Reed, R.K.; Aukland, K. Interstitial Fluid Pressure in Rats Measured With a Modified Wick Technique. *MlCROVASCLJLAR RESEARCH* **1977**, *14*, 27–36, doi:https://doi.org/10.1016/0026-2862(77)90138-8.

144. Wiederhielm, C.A.; Woodbury, J.W.; Kirk, S.; Rushmer, R.F. Pulsatile Pressures in the Microcirculation of Frog’s Mesentery’. *AM J Physiol* **1964**, *207*, 173–176, doi:10.1152/ajplegacy.1964.207.1.173.

145. Trautner, B.W.; Darouiche, R.O. Catheter-Associated Infections Pathogenesis Affects Prevention. *Arch Intern Med* **2004**, *164*, 842–850, doi:10.1001/archinte.164.8.842.

146. Eggimann, P.; Sax, H.; Pittet, D. Catheter-Related Infections. *Microbes Infect* **2004**, *6*, 1033–1042, doi:10.1016/j.micinf.2004.05.018.

147. Masu, K.; Machida, K.; Yamane, D.; Judy, J.W. Microelectromechanical Systems (MEMS):Fabrication, Design and Applications. *Smart Mater. Struct* **2001**, *10*, 1115, doi:10.1088/0964-1726/10/6/301.

148. Kumar, S.S.; Pant, B.D. Design Principles and Considerations for the “ideal” Silicon Piezoresistive Pressure Sensor: A Focused Review. *Microsystem Technologies* **2014**, *20*, 1213–1247, doi:10.1007/s00542-014-2215-7.

149. Jeong, S.; Kim, Y.; Kim, G.; Blaauw, D. A Pressure Sensing System with ±0.75 MmHg (3σ) Inaccuracy for Battery-Powered Low Power IoT Applications. *2020 IEEE Symposium on VLSI Circuits,* **2020**, 1–2, doi:10.1109/VLSICircuits18222.2020.9162778.

150. Mejia-Aranda, A.R.; Basurto-Pensado, M.A.; Antunez-Ceron, E.E.; Castro-Gómez, L.L.; Urquiza-Beltran, G.; Rodriguez, J.A.; García, J.C.; Sánchez-Mondragón, J.J.; Ruiz-Pérez, V.I. Fiber Optic Pressure Sensor of 0-0.36 Psi by Multimode Interference Technique. *Journal of Applied Research and Technology* **2013**, *11*, 695–701, doi:https://doi.org/10.1016/S1665-6423(13)71577-3.

151. Chen, Z.; Wang, Z.; Li, X.; Lin, Y.; Luo, N.; Long, M.; Zhao, N.; Xu, J. Bin Flexible Piezoelectric-Induced Pressure Sensors for Static Measurements Based on Nanowires/Graphene Heterostructures. *ACS Nano* **2017**, *11*, 4507–4513, doi:10.1021/acsnano.6b08027.

152. Cai, M.X.; Yang, Y.J. A Wireless Cardiovascular Pressure Sensor Based on an Iontronic Film with High Sensitivity. In Proceedings of the Proceedings of the IEEE International Conference on Micro Electro Mechanical Systems (MEMS); Institute of Electrical and Electronics Engineers Inc., January 25 2021; Vol. 2021-January, pp. 135–138.

153. Tai, Y.; Yang, Z. Toward Flexible Wireless Pressure-Sensing Device via Ionic Hydrogel Microsphere for Continuously Mapping Human-Skin Signals. *Adv Mater Interfaces* **2017**, *4*, doi:10.1002/admi.201700496.

154. Song, S.H.; Brown, M.; Maleki, T.; Ziaie, B. A Wireless Interstitial Pressure Sensor with a Guyton Chamber. In Proceedings of the 2013 Transducers and Eurosensors XXVII: The 17th International Conference on Solid-State Sensors, Actuators and Microsystems, TRANSDUCERS and EUROSENSORS 2013; 2013; pp. 2161–2164.

155. Song, P.; Ma, Z.; Ma, J.; Yang, L.; Wei, J.; Zhao, Y.; Zhang, M.; Yang, F.; Wang, X. Recent Progress of Miniature MEMS Pressure Sensors. *Micromachines (Basel)* 2020, *11*.

156. Wang, X.; Liu, Z.; Zhang, T. Flexible Sensing Electronics for Wearable/Attachable Health Monitoring. *Small* 2017, *13*.

157. Xu, F.; Li, X.; Shi, Y.; Li, L.; Wang, W.; He, L.; Liu, R. Recent Developments for Flexible Pressure Sensors: A Review. *Micromachines (Basel)* 2018, *9*, 580.

158. Sun, Z.; Fang, H.; Xu, B.; Yang, L.; Niu, H.; Wang, H.; Chen, D.; Liu, Y.; Wang, Z.; Wang, Y.; et al. Flexible Wireless Passive Lc Pressure Sensor with Design Methodology and Cost-Effective Preparation. *Micromachines (Basel)* **2021**, *12*, 976, doi:10.3390/mi12080976.

159. Nie, B.; Huang, R.; Yao, T.; Zhang, Y.; Miao, Y.; Liu, C.; Liu, J.; Chen, X. Textile-Based Wireless Pressure Sensor Array for Human-Interactive Sensing. *Adv Funct Mater* **2019**, *29*, 1808786, doi:10.1002/adfm.201808786.

160. Palmroth, A.; Salpavaara, T.; Lekkala, J.; Kellomäki, M. Fabrication and Characterization of a Wireless Bioresorbable Pressure Sensor. *Adv Mater Technol* **2019**, *4*, 1900428, doi:10.1002/admt.201900428.

161. Zhai, Y.; Lee, J.; Hoang, Q.; Sievenpipper, D.; Garudadri, H.; Ng, T.N. A Printed Wireless Fluidic Pressure Sensor. *Flexible and Printed Electronics* **2018**, *3*, 035006, doi:10.1088/2058-8585/aae09e.

162. Lu, D.; Yan, Y.; Deng, Y.; Yang, Q.; Zhao, J.; Seo, M.H.; Bai, W.; MacEwan, M.R.; Huang, Y.; Ray, W.Z.; et al. Bioresorbable Wireless Sensors as Temporary Implants for In Vivo Measurements of Pressure. *Adv Funct Mater* **2020**, *30*, 2003754, doi:10.1002/adfm.202003754.

163. Kou, H.; Zhang, L.; Tan, Q.; Liu, G.; Dong, H.; Zhang, W.; Xiong, J. Wireless Wide-Range Pressure Sensor Based on Graphene/PDMS Sponge for Tactile Monitoring. *Sci Rep* **2019**, *9*, 3916, doi:10.1038/s41598-019-40828-8.

164. Farooq, M.; Iqbal, T.; Vazquez, P.; Farid, N.; Thampi, S.; Wijns, W.; Shahzad, A. Thin-Film Flexible Wireless Pressure Sensor for Continuous Pressure Monitoring in Medical Applications. *Sensors (Switzerland)* **2020**, *20*, 6653, doi:10.3390/s20226653.

165. Chen, L.Y.; Tee, B.C.K.; Chortos, A.L.; Schwartz, G.; Tse, V.; J. Lipomi, D.; Wong, H.S.P.; McConnell, M. V.; Bao, Z. Continuous Wireless Pressure Monitoring and Mapping with Ultra-Small Passive Sensors for Health Monitoring and Critical Care. *Nat Commun* **2014**, *5*, 5028, doi:10.1038/ncomms6028.

166. Li, W.; Liu, A.; Wang, Y.; Qu, K.; Wen, H.; Zhao, J.; Shi, Y.; Wang, H.; Ye, M.; Guo, W. Implantable and Degradable Wireless Passive Protein-Based Tactile Sensor for Intracranial Dynamic Pressure Detection. *Electronics (Switzerland)* **2023**, *12*, 2466, doi:10.3390/electronics12112466.

167. Boutry, C.M.; Beker, L.; Kaizawa, Y.; Vassos, C.; Tran, H.; Hinckley, A.C.; Pfattner, R.; Niu, S.; Li, J.; Claverie, J.; et al. Biodegradable and Flexible Arterial-Pulse Sensor for the Wireless Monitoring of Blood Flow. *Nat Biomed Eng* **2019**, *3*, 47–57, doi:10.1038/s41551-018-0336-5.

168. Jia, P.; Liu, J.; Qian, J.; Ren, Q.; An, G.; Xiong, J. An LC Wireless Passive Pressure Sensor Based on Single-Crystal MgO MEMS Processing Technique for High Temperature Applications. *Sensors* **2021**, *21*, 6602, doi:10.3390/s21196602.

169. Zheng, C.; Li, W.; Li, A.L.; Zhan, Z.; Wang, L.Y.; Sun, D.H. Design and Manufacturing of a Passive Pressure Sensor Based on LC Resonance. *Micromachines (Basel)* **2016**, *7*, 87, doi:10.3390/mi7050087.

170. Lucarotti, C.; Oddo, C.M.; Vitiello, N.; Carrozza, M.C. Synthetic and Bio-Artificial Tactile Sensing: A Review. *Sensors (Switzerland)* 2013, *13*, 1435–1466.

171. Li, J.; Bao, R.; Tao, J.; Peng, Y.; Pan, C. Recent Progress in Flexible Pressure Sensor Arrays: From Design to Applications. *J Mater Chem C Mater* 2018, *6*, 11878–11892.

172. Zang, Y.; Zhang, F.; Di, C.A.; Zhu, D. Advances of Flexible Pressure Sensors toward Artificial Intelligence and Health Care Applications. *Mater Horiz* 2015, *2*, 140–156.

173. Nopper, R.; Niekrawietz, R.; Reindl, L. Wireless Readout of Passive LC Sensors. *IEEE Trans Instrum Meas* **2010**, *59*, 2450–2457, doi:10.1109/TIM.2009.2032966.

174. Nopper, R.; Has, R.; Reindl, L. A Wireless Sensor Readout System-Circuit Concept, Simulation, and Accuracy. In Proceedings of the IEEE Transactions on Instrumentation and Measurement; August 2011; Vol. 60, pp. 2976–2983.

175. Fonseca, M.A.; English, J.M.; Von Arx, M.; Allen, M.G. Wireless Micromachined Ceramic Pressure Sensor for High-Temperature Applications. *Journal of Microelectromechanical Systems* **2002**, *11*, 337–343, doi:10.1109/JMEMS.2002.800939.

176. Stauffer, F.; Zhang, Q.; Tybrandt, K.; Llerena Zambrano, B.; Hengsteler, J.; Stoll, A.; Trüeb, C.; Hagander, M.; Sujata, J.M.; Hoffmann, F.; et al. Soft Electronic Strain Sensor with Chipless Wireless Readout: Toward Real-Time Monitoring of Bladder Volume. *Adv Mater Technol* **2018**, *3*, 1800031, doi:10.1002/admt.201800031.

177. Jain, S.; Pandey, K.; Lahoti, A.; Rao, Pk. Evaluation of Skin and Subcutaneous Tissue Thickness at Insulin Injection Sites in Indian, Insulin Naïve, Type-2 Diabetic Adult Population. *Indian J Endocrinol Metab* **2013**, *17*, 864–870, doi:10.4103/2230-8210.117249.

178. Deng, W.J.; Wang, L.F.; Dong, L.; Huang, Q.A. Symmetric LC Circuit Configurations for Passive Wireless Multifunctional Sensors. *Journal of Microelectromechanical Systems* **2019**, *28*, 344–350, doi:10.1109/JMEMS.2019.2901818.

179. Deng, W.J.; Wang, L.F.; Dong, L.; Huang, Q.A. LC Wireless Sensitive Pressure Sensors with Microstructured PDMS Dielectric Layers for Wound Monitoring. *IEEE Sens J* **2018**, *18*, 4886–4892, doi:10.1109/JSEN.2018.2831229.

180. Dautta, M.; Alshetaiwi, M.; Escobar, A.; Torres, F.; Bernardo, N.; Tseng, P. Multi-Functional Hydrogel-Interlayer RF/NFC Resonators as a Versatile Platform for Passive and Wireless Biosensing. *Adv Electron Mater* **2020**, *6*, 1901311, doi:10.1002/aelm.201901311.

181. Zhang, H.; Han, W.; Xu, K.; Zhang, Y.; Lu, Y.; Nie, Z.; Du, Y.; Zhu, J.; Huang, W. Metallic Sandwiched-Aerogel Hybrids Enabling Flexible and Stretchable Intelligent Sensor. *Nano Lett* **2020**, *20*, 3449–3458, doi:10.1021/acs.nanolett.0c00372.

182. Luu, T.P.; He, Y.; Brown, S.; Nakagame, S.; Contreras-Vidal, J.L. Gait Adaptation to Visual Kinematic Perturbations Using a Real-Time Closed-Loop Brain-Computer Interface to a Virtual Reality Avatar. *J Neural Eng* **2016**, *13*, doi:10.1088/1741-2560/13/3/036006.

183. Horak, F.; King, L.; Mancini, M.; Horak, F.; King, L.; Mancini, M.; Role, M.M. *Role of Body-Worn Movement Monitor Technology for Balance and Gait Rehabilitation Innovative Technologies Special Series Post a Rapid Response To*; 2015; Vol. 95;.

184. Xiao, Y.; Zhang, Z.; Beck, A.; Yuan, J.; Thalmann, D. *Human-Robot Interaction by Understanding Upper Body Gestures*;

185. Bonnet, V.; Joukov, V.; Kulić, D.; Fraisse, P.; Ramdani, N.; Venture, G. Monitoring of Hip and Knee Joint Angles Using a Single Inertial Measurement Unit during Lower Limb Rehabilitation. *IEEE Sens J* **2016**, *16*, 1557–1564, doi:10.1109/JSEN.2015.2503765.

186. Wang, Q.; Markopoulos, P.; Yu, B.; Chen, W.; Timmermans, A. Interactive Wearable Systems for Upper Body Rehabilitation: A Systematic Review. *J Neuroeng Rehabil* 2017, *14*.

187. Stetter, B.J.; Ringhof, S.; Krafft, F.C.; Sell, S.; Stein, T. Estimation of Knee Joint Forces in Sport Movements Using Wearable Sensors and Machine Learning. *Sensors (Switzerland)* **2019**, *19*, doi:10.3390/s19173690.

188. Eichelberger, P.; Ferraro, M.; Minder, U.; Denton, T.; Blasimann, A.; Krause, F.; Baur, H. Analysis of Accuracy in Optical Motion Capture – A Protocol for Laboratory Setup Evaluation. *J Biomech* **2016**, *49*, 2085–2088, doi:10.1016/j.jbiomech.2016.05.007.

189. Herda, L.; Fua, P.; Pl⍰, R.; Boulic, R.; Thalmann, D. *Using Skeleton-Based Tracking to Increase the Reliability of Optical Motion Capture*; 2001; Vol. 20;.

190. Stone, E.E.; Skubic, M. Unobtrusive, Continuous, in-Home Gait Measurement Using the Microsoft Kinect. *IEEE Trans Biomed Eng* **2013**, *60*, 2925–2932, doi:10.1109/TBME.2013.2266341.

191. Ferryanto, F.; Nakashima, M. Development of a Markerless Optical Motion Capture System for Daily Use of Training in Swimming. *Sports Engineering* **2017**, *20*, 63–72, doi:10.1007/s12283-016-0218-6.

192. Mani, N.; Haridoss, P.; George, B. A Wearable Ultrasonic-Based Ankle Angle and Toe Clearance Sensing System for Gait Analysis. *IEEE Sens J* **2021**, *21*, 8593–8603, doi:10.1109/JSEN.2020.3047900.

193. Majumder, S.; Jamal Deen, M. Wearable IMU-Based System for Real-Time Monitoring of Lower-Limb Joints. *IEEE Sens J* **2021**, *21*, 8267–8275, doi:10.1109/JSEN.2020.3044800.

194. Jeong, S.M.; Son, M.; Kang, Y.; Yang, J.; Lim, T.; Ju, S. Development of Multi-Angle Fiber Array for Accurate Measurement of Flexion and Rotation in Human Joints. *npj Flexible Electronics* **2021**, *5*, doi:10.1038/s41528-021-00131-x.

195. Qin, H.; Hajiaghajani, A.; Escobar, A.R.; Zargari, A.H.A.; Jimenez, A.; Kurdahi, F.; Tseng, P. Laser-Induced Graphene-Based Smart Textiles for Wireless Cross-Body Metrics. *ACS Appl Nano Mater* **2023**, *6*, 19158–19167, doi:10.1021/acsanm.3c03582.

196. Tian, X.; Lee, P.M.; Tan, Y.J.; Wu, T.L.Y.; Yao, H.; Zhang, M.; Li, Z.; Ng, K.A.; Tee, B.C.K.; Ho, J.S. Wireless Body Sensor Networks Based on Metamaterial Textiles. *Nat Electron* **2019**, *2*, 243–251, doi:10.1038/s41928-019-0257-7.

197. Tian, X.; Zeng, Q.; Nguyen, D.T.; Ho, J.S. Textile-Integrated Phased Surfaces for Wireless Networking of Bioelectronic Devices. *IEEE Trans Antennas Propag* **2024**, *72*, 267–276, doi:10.1109/TAP.2023.3322752.

198. Lin, R.; Kim, H.J.; Achavananthadith, S.; Xiong, Z.; Lee, J.K.W.; Kong, Y.L.; Ho, J.S. Digitally-Embroidered Liquid Metal Electronic Textiles for Wearable Wireless Systems. *Nat Commun* **2022**, *13*, doi:10.1038/s41467-022-29859-4.

199. Hajiaghajani, A.; Tseng, P. Microelectronics-Free, Augmented Telemetry from Body-Worn Passive Wireless Sensors. *Adv Mater Technol* **2021**, *6*, doi:10.1002/admt.202001127.

200. Aoki, T.; Dayan, B.; Wilcut, E.; Bowen, W.P.; Parkins, A.S.; Kippenberg, T.J.; Vahala, K.J.; Kimble, H.J. Observation of Strong Coupling between One Atom and a Monolithic Microresonator. *Nature* **2006**, *443*, 671–674, doi:10.1038/nature05147.

201. Niu, S.; Matsuhisa, N.; Beker, L.; Li, J.; Wang, S.; Wang, J.; Jiang, Y.; Yan, X.; Yun, Y.; Burnett, W.; et al. A Wireless Body Area Sensor Network Based on Stretchable Passive Tags. *Nat Electron* **2019**, *2*, 361–368, doi:10.1038/s41928-019-0286-2.

202. Dautta, M.; Hajiaghajani, A.; Ye, F.; Escobar, A.R.; Jimenez, A.; Dia, K.K.H.; Tseng, P. Programmable Multiwavelength Radio Frequency Spectrometry of Chemophysical Environments through an Adaptable Network of Flexible and Environmentally Responsive, Passive Wireless Elements. *Small Science* **2022**, *2*, doi:10.1002/smsc.202200013.

203. Dautta, M.; Dia, K.K.H.; Hajiaghajani, A.; Escobar, A.R.; Alshetaiwi, M.; Tseng, P. Multiscale, Nano- to Mesostructural Engineering of Silk Biopolymer-Interlayer Biosensors for Continuous Comonitoring of Nutrients in Food. *Adv Mater Technol* **2022**, *7*, doi:10.1002/admt.202100666.

204. Stevens, C.J. Magnetoinductive Waves and Wireless Power Transfer. *IEEE Trans Power Electron* **2015**, *30*, 6182–6190, doi:10.1109/TPEL.2014.2369811.

205. Zhang, F.; Hackworth, S.A.; Fu, W.; Li, C.; Mao, Z.; Sun, M. Relay Effect of Wireless Power Transfer Using Strongly Coupled Magnetic Resonances. *IEEE Trans Magn* **2011**, *47*, 1478–1481, doi:10.1109/TMAG.2010.2087010.

206. Hajiaghajani, A.; Rwei, P.; Afandizadeh Zargari, A.H.; Escobar, A.R.; Kurdahi, F.; Khine, M.; Tseng, P. Amphibious Epidermal Area Networks for Uninterrupted Wireless Data and Power Transfer. *Nat Commun* **2023**, *14*, doi:10.1038/s41467-023-43344-6.

207. Mishra, V.; Kiourti, A. Wearable Electrically Small Loop Antennas for Monitoring Joint Flexion and Rotation. *IEEE Trans Antennas Propag* **2020**, *68*, 134–141, doi:10.1109/TAP.2019.2935147.

208. Saltzman, H.; Rajaram, R.; Zhang, Y.; Islam, M.A.; Kiourti, A. Wearable Loops for Dynamic Monitoring of Joint Flexion: A Machine Learning Approach. *Electronics (Switzerland)* **2024**, *13*, doi:10.3390/electronics13122245.

209. Liu, N.; Langguth, L.; Weiss, T.; Kästel, J.; Fleischhauer, M.; Pfau, T.; Giessen, H. Plasmonic Analogue of Electromagnetically Induced Transparency at the Drude Damping Limit. *Nat Mater* **2009**, *8*, 758–762, doi:10.1038/nmat2495.

210. Liu, N.; Weiss, T.; Mesch, M.; Langguth, L.; Eigenthaler, U.; Hirscher, M.; Sönnichsen, C.; Giessen, H. Planar Metamaterial Analogue of Electromagnetically Induced Transparency for Plasmonic Sensing. *Nano Lett* **2010**, *10*, 1103–1107, doi:10.1021/nl902621d.

211. Çetin, A.E.; Artar, A.; Turkmen, M.; Ali Yanik, A.; Altug, H.; Boller, K.J.; Imamolu, A.; Harris, S.E.; Hau, L. V; Dutton, Z.; et al. *5740) Resonance; (260.2110) Electromagnetic Optics; (160.4760) Optical Properties*; 1991; Vol. 66;.

212. Part, B. Caretaker4 User Manual Caretaker4. **2018**, *0*.

213. Abiri, A.; Chou, E.F.; Qian, C.; Rinehart, J.; Khine, M. Intra-Beat Biomarker for Accurate Continuous Non-Invasive Blood Pressure Monitoring. *Sci Rep* **2022**, *12*, doi:10.1038/s41598-022-19096-6.

214. Chung, H.U.; Rwei, A.Y.; Hourlier-Fargette, A.; Xu, S.; Lee, K.H.; Dunne, E.C.; Xie, Z.; Liu, C.; Carlini, A.; Kim, D.H.; et al. Skin-Interfaced Biosensors for Advanced Wireless Physiological Monitoring in Neonatal and Pediatric Intensive-Care Units. *Nat Med* **2020**, *26*, 418–429, doi:10.1038/s41591-020-0792-9.

215. Abiri, A.; Chou, E.F.; Shen, W.; Fisher, M.J.; Khine, M. Changes in Beat-to-Beat Blood Pressure and Pulse Rate Variability Following Stroke. *Sci Rep* **2023**, *13*, doi:10.1038/s41598-023-45479-4.

216. Zheng, Y.-Q.; Liu, Y.; Zhong, D.; Nikzad, S.; Liu, S.; Yu, Z.; Liu, D.; Wu, H.-C.; Zhu, C.; Li, J.; et al. Monolithic Optical Microlithography of High-Density Elastic Circuits. *Science (1979)* **2021**, *373*, 88–94, doi:10.1126/science.abh3551.